Quantum Transport in the Presence of a Local Time-Periodic Potential in a Magnetic Field

by

Kristinn Torfason

VERKFRÆÐI- OG NÁTTÚRUVÍSINDASVIÐ /
SCHOOL OF ENGINEERING AND
NATURAL SCIENCES

HÁSKÓLI ÍSLANDS / UNIVERSITY OF ICELAND

University of Iceland School of Engineering and Natural Science
Faculty of Physical Science
Department of Physics

RH-02-2009

Quantum Transport in the Presence of a Local Time-Periodic Potential in a Magnetic Field

by

Kristinn Torfason

UNIVERSITY OF ICELAND
SCHOOL OF ENGINEERING AND NATURAL SCIENCES

A thesis submitted in partial fulfilment of
the requirements for the degree of Master of
Science in Physics at the University of Iceland

Committee in charge:
Viðar Guðmundsson, Chair
Sigurður Ingi Erlingsson

Reykjavík
May 2009

Quantum Transport in the Presence of a Local Time-Periodic Potential in a Magnetic Field

Abstract

The transport through a quantum wire is investigated with an embedded time-periodic Gaussian-shaped potential, a static single Quantum Point Contact and a double Quantum Point Contact with and without a homogeneous perpendicular magnetic field. A mixed momentum-coordinate representation is used to obtain a coupled integral equation called the Lippmann-Schwinger equation. Numerical calculations are used to solve this equation which couples both the subbands and the sidebands in the system. The Landauer-Büttiker formalism is then used to calculate the conductance of the system. The numerical results show dip-and-peak structures in the conductance in the time-dependent case when the incident electrons can make inelastic transitions to a subband edge. They also show result obtained in the static case such as quasi-bound states, mode mixing, Aharonov-Bohm oscillations and edge states in a magnetic field.

Ágrip

Flutningur rafeinda í gegnum skammtavír með Gaussísku mætti sem er lotubundið í tíma, tíma-óháða punktsnertu og tvöfalda punktsnertu með og án einsleitu segulsviði hornréttu á vírinn er rannsakað. Notast er við blandaða hverfiþunga-rúm framsetningu til þess að fá heildis-jöfnu sem kallast Lippmann-Schwinger jafna. Tölulegum útreikningum er beitt til þess að leysa jöfnuna sem tengir saman bæði undirborða og hliðarborða vírsins. Landauer-Büttiker framsetningin er síðan notuð til að reikna leiðnina í gegnum kerfið. Útreikningarnir sýna bæði dali og hóla í leiðninni í tíma-háða tilvikinu þegar rafeindir í vírnum lenda í ófjaðrandi árekstrum við mættið. Þeir sýna einnig hegðun sem sjást í tíma-óháðum reikningum eins og hálf-bundin ástönd, blöndun undirborða, Aharonov-Bohm sveiflur og jaðar-ástönd í segulsviði.

If I have seen farther than others, it has
been by standing on the shoulders of giants.

Sir Isaac Newton.

Preface and Acknowledgement's

This thesis was written as a partial requirement for the degree of Master of Science at the University of Iceland. It is a detailed summary of the work I did from the year 2007 to 2009 while working at the Science Institute of the University of Iceland. This work was supervised by Prof. Viðar Guðmundsson at the Science Institute and was partly funded by a research grant from the Science and Technology Research Programme for Postgenomic Biomedicine Nanoscience and Nanotechnology.

I would like to take the opportunity to thank Viðar Guðmundsson for his guidance in this work. His willingness to help, experience and interest in physics has been an inspiration. I would also like thank Chi-Shung Tang at the National United University in Taiwan for his helpfull comments and cooperation in this work.

Last but not least I would like to thank my family for their love and support. With out their help and encouragement to continue my studies I would have never made it this far.

Contents

List of Figures

List of Tables

CHAPTER 1

Introduction

Electronic devices today are getting smaller and smaller while at the same time there are demands that they use less power and have more functionality. Manufacturers have so far been able to keep up with these demands by making the elements that make up such devices smaller. This miniaturisation process is not without its flaws, when the size of the circuit elements starts approaching the atomic scale quantum effects become more important. There will come a point where it is no longer possible to continue this miniaturisation of existing semiconductor devices and new devices must be made from the ground up. These new devices must be modeled using quantum mechanics in order to take into account the quantum effects.

Low-dimensional devices are structures that are confined in one, two or three dimensions. This confinement gives rise to discrete energy bands in the direction of the confinement, usually referred to as subbands. Quantum effects such as this are an inherit part of these nanostructures, but in order to see the full wave nature of the electrons they must be cooled to sufficiently low temperatures. With today's refrigeration technology it is no problem to cool these devices to sufficiently low temperatures and interesting quantum effects have been predicted and observed in transport through such structures. One such effect is scattering between subbands [1] in a quantum wire with embedded static potentials. The subbands can either be propagating or non-propagating if the corresponding wave-vector is real or imaginary respectively. Scattering can occur into both propagating or non-propagating modes which are then evanescent [2]. Many more effects have been observed that can change the transport through the structure, such as Aharonov-Bohm oscillations in a magnetic field [3] and quasi-bound states in quantum dots [4].

Inelastic scatterings can also be introduced with time-dependent potentials. When the Hamiltonian is time dependent the system is no longer a conservative one, i.e. conservation of energy is broken. It turns out that when working with a periodic Hamiltonian that energy is gained and lost in discreet quantum [5] of $\hbar\omega$, where ω is the frequency of the potential. This introduces sidebands to the energy spectrum as the electrons can have energies $E_0 \pm m\hbar\omega$, where m is the sideband index and E_0 the incident energy. Such systems are of great interest because of their ability to pump a certain number of electrons through the system during one period. This quantisation of the particle transport is not new and was first thought of by Thouless [6] in 1983. This field is generally referred to as Quantum Pumping and may have many applications in Quantum Computing and Quantum Information processing where a certain number of electrons is required to perform a given task.

If one wants to manufacture a low-dimensional device the usual starting point is a two-dimensional electron gas (2DEG). A 2DEG can be made at the interface of a GaAs/$Ga_{1-x}Al_xAs$ heterostructure [7] as seen in Fig. 1.1. It is possible to grow such structures one atomic layer at a time using techniques such as Atomic Layer Deposition (ALD) or molecular beam epitaxy (MBE). The confinement and other potentials can then be electrostatically induced by use of gates deposited on top of the heterostructure.

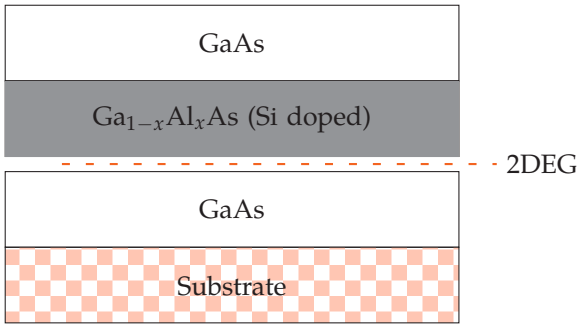

FIG. 1.1: GaAs/$Ga_{1-x}Al_xAs$ heterostructure used to make a 2DEG.

CHAPTER 2

Theory

This chapter explains the basic theory behind electron transport through a quantum wire with embedded potentials that are both static and time-harmonic. The first section is a general discussion about transport in quantum wires and shows how the conductance can be calculated using the Landauer-Büttiker formula. In the next section the Lippmann-Schwinger scattering formalism is used to find an equation for the wave function of the system. The third section show how the transmission coefficients that are needed to calculate the conductance with the Landauer-Büttiker formula are found from the asymptotic form of the wave function. The chapter then concludes with a discussion on the form of the potential and its effects on the transport.

2.1 Transport in Quantum Wires

The usual setup for quantum wires is a sample connected to two electron reservoirs, a drain and source via leads. This setup can be seen in Fig. 2.1, where we have the source on the left, the drain on the right, and in the middle a scattering potential which we will assume is time-dependent. The electrons will be fed into the sample from the source on

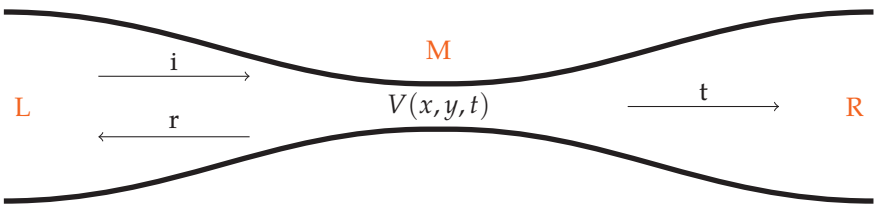

FIG. 2.1: The standard geometry for quantum wires. Two contacts, source (L) and drain (R), connected to a sample (M).

the left where they travel along the lead in the x-direction to the scattering area (M) in the middle. There they are either scattered back into the source or transmitted into the drain. The electrons will be confined in the y-direction by a confinement potential. This confinement gives rise to eigenstates $\phi_n(y)$ that are solutions to the eigenvalue equation

$$\left[-\frac{\hbar^2}{2m^*}\frac{\mathrm{d}^2}{\mathrm{d}y^2} + V_c(y)\right]\phi_n(y) = E_n\phi_n(y)\,, \tag{2.1}$$

where $V_c(y)$ is the confinement potential that we will leave unspecified for the time being. In the leads far away from the scattering region the scattering potential will be zero and the wave function will be a solution of the equation

$$i\hbar\frac{\partial}{\partial t}\psi(x,y,t) = \left[-\frac{\hbar^2}{2m^*}\nabla^2 + V_c(y)\right]\psi(x,y,t) \tag{2.2}$$

We shall expand the time-depended part of the wave function in a Fourier series with frequency ω,

$$\psi(x,y,t) = \sum_m \psi^m(x,y)e^{i(E_0/\hbar+m\omega)t}\,, \tag{2.3}$$

where we have added a global phase-factor $e^{i(E_0/\hbar)t}$ to represent the total energy of the incident electron. The index m has a physical meaning if the potential is time-harmonic [5] and is generally referred to as the sideband index. It labels the possible states that electrons can be inelastically scattered into, these states are usually called sidebands. It can be easily seen that $\psi^m(x,y)$ is a solution of the equation

$$\left[-\frac{\hbar^2}{2m^*}\left(\frac{\partial^2}{\partial x^2}+\frac{\partial^2}{\partial y^2}\right) + V_c(y)\right]\psi^m(x,y) = (E_0+\hbar m\omega)\psi^m(x,y)\,. \tag{2.4}$$

We now expand $\psi^m(x,y)$ in the eigenfunctions of the confinement potential

$$\psi^m(x,y) = \sum_n \varphi_n^m(x)\phi_n(y)\,, \tag{2.5}$$

where $\varphi_n^m(x)$ are the coefficients of the expansion. It should now be obvious from Eq. (2.4) that the expansion coefficients are just the eigenfunctions for a free particle in the x-direction with coefficient that depend on n and m,

$$\psi(x,y,t) = \sum_m\sum_n c_n^m e^{i(E_0/\hbar+m\omega)t}e^{\pm ik_n^m x}\phi_n(y)\,. \tag{2.6}$$

Here k_n^m is the wave-vector for the propagation in the x-direction given by

$$\frac{\hbar^2(k_n^m)^2}{2m^*} = E+\hbar m\omega - E_n\,, \qquad \text{i.e.} \qquad k_n^m = \sqrt{\frac{2m^*}{\hbar^2}(E+\hbar m\omega - E_n)}\,. \tag{2.7}$$

Figure 2.2 is a graphical description of Eq. (2.7) and shows the possible scatterings

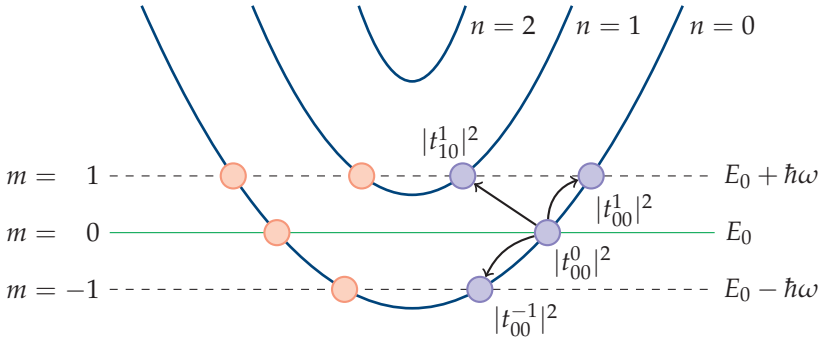

FIG. 2.2: A graphical representation of the dispersion relation in the leads.

processes for a particle incoming in the lowest subband and sideband $m = 0$. A scattering between two points on the same line are elastic while jumps between different lines represent inelastic scattering that are induced by a time-dependent potential. An elastic jump can result in an evanescent mode as can be seen from Eq. (2.7). If E_n is changed in such a way that $E + \hbar m\omega < E_n$ with m fixed, then the resulting wave-vector will be imaginary, resulting in an evanescent state that decays exponentially into the leads.

Finding the wave function in the scattering region can be a difficult task and must usually by done numerically, as it depends on the scattering potential. However, in order to discuss the conductance through the system we do not need to know the exact form of the scattering wave function. We will therefore discuss its derivation later in the chapter.

The total wave function of the system will have the form

$$\Psi_E(x,y,t) = \begin{cases} \sum_m \sum_n \left\{ a_n^m e^{i(E_0/\hbar + m\omega)t} e^{ik_n^m x} \phi_n(y) + b_n^m e^{i(E_0/\hbar+m\omega)t} e^{-ik_n^m x} \phi_n(y) \right\}, & (x,y) \in L, \\ \Psi_{M,E}(x,y,t), & (x,y) \in M, \\ \sum_m \sum_n \left\{ c_n^m e^{i(E_0/\hbar+m\omega)t} e^{-ik_n^m x} \phi_n(y) + d_n^m e^{i(E_0/\hbar+m\omega)t} e^{ik_n^m x} \phi_n(y) \right\}, & (x,y) \in R, \end{cases} \quad (2.8)$$

where a_n^m, b_n^m, c_n^m and d_n^m are unknown coefficients. We now define a scattering state

$$\psi_n(x,y,t) = \begin{cases} e^{i(E_0/\hbar)t} e^{ik_n^0 x} \phi_n(y) + \sum_{m'} \sum_{n'} r_{n'n}^{m'0} e^{i(E_0/\hbar+m'\omega)t} e^{-ik_{n'}^{m'} x} \phi_{n'}(y), & (x,y) \in L, \\ \psi_{M,E}(x,y,t), & (x,y) \in M, \\ \sum_{m'} \sum_{n'} t_{n'n}^{m'0} e^{i(E_0/\hbar+m'\omega)t} e^{ik_{n'}^{m'} x} \phi_{n'}(y), & (x,y) \in R. \end{cases} \quad (2.9)$$

In the scattering state we have chosen to have an incoming wave (electron) from the left with energy E_0 in subband n. These waves or electrons scatter into subband n' and sideband m' in either the left lead with probability $|r_{n'n}^{m'}|^2$ or the right one with probability $|t_{n'n}^{m'}|^2$. These coefficients are usually called reflection ($r_{n'n}^{m'}$) and transmission ($t_{n'n}^{m'}$) coefficient as they determine the probability for reflection and transmission.

The Landauer-Büttiker formula connects the transmission coefficients to the conductance of the system. It states that each subband should contribute a factor $\frac{2e^2}{h} T_n$ to the conductance,

hence in our case the conductance is given by

$$G(\mu) = \frac{2e^2}{h} \sum_{m'} \mathbf{Tr}\left[(\mathbf{t}^{m'})^\dagger \mathbf{t}^{m'} \right] , \tag{2.10}$$

where $\mathbf{t}^{m'}$ is the matrix equivalent of the transmission coefficients $(t^{m'}_{n'n})$,

$$\mathbf{t}^{m'} = \begin{pmatrix} t^{m'}_{11} & t^{m'}_{12} & \dots & t^{m'}_{1n} \\ t^{m'}_{21} & \ddots & & \vdots \\ \vdots & & \ddots & \vdots \\ t^{m'}_{n'1} & \dots & \dots & t^{m'}_{n'n} \end{pmatrix} . \tag{2.11}$$

2.2 The Lippmann-Schwinger Equation

In this section we aim to find the so called Lippmann-Schwinger equation for the wave function. We extend the Lippmann-Schwinger approach to include time-periodic potentials and keep it general to be able to apply it to any reasonable localised potential. When the wave function for the system has been found we can read from the asymptotic form the transmission and reflection coefficients and use them to calculate the conductance of the system with Eq. (2.10).

Our starting point is the two-dimensional time-dependent Schrödinger equation

$$i\hbar \frac{\partial}{\partial t} \Psi(x,y,t) = H(t)\Psi(x,y,t) , \tag{2.12}$$

where the Hamiltonian is given by

$$H(t) = \frac{p^2}{2m^*} + V_c(y) + V(x,y,t) .$$

Here $V_c(y)$ is the confinement potential which we choose to be parabolic and $V(x,y,t)$ is a general time-periodic potential that we will leave unspecified for now.

We want to have a homogeneous magnetic field in the z-direction. We will therefore have to choose a gauge and replace the momentum operator with the effective momentum operator in a magnetic field,

$$p_x = -i\hbar \frac{\partial}{\partial x} \quad \rightarrow \quad \pi_x = -i\hbar \frac{\partial}{\partial x} + eA_x .$$

The gauge we choose is the Landau gauge where $\vec{A} = -By\vec{x}$, giving us

$$i\hbar \partial_t \Psi(x,y,t) = \left\{ -\frac{\hbar^2}{2m^*} \left(\nabla^2 - \frac{2i}{l^2} y\partial_x - \frac{y^2}{l^4} \right) + \frac{1}{2} m^* \Omega_0^2 y^2 + V(x,y,t) \right\} \Psi(x,y,t) . \tag{2.13}$$

The constant l is called the magnetic length and is given by

$$l^2 = \frac{\hbar}{eB} .$$

Equation (2.13) is coupled in the x- and y-direction, but we do expect to be able to separate the equation in momentum-coordinate space [8] because the wire is homogeneous in the x-direction. Therefore, we do a Fourier transform with respect to the x-coordinate of the wave function,

$$\Psi(x,y,t) = \int \frac{\mathrm{d}p}{2\pi}\, e^{ipx}\Psi(p,y,t) \quad , \quad \Psi(p,y,t) = \int \mathrm{d}x\, e^{-ipx}\Psi(x,y,t)\,. \tag{2.14}$$

Inserting the above into the Schrödinger equation and then transforming the equation with

$$\int \mathrm{d}x\, e^{-iqx}\,,$$

we obtain an equation for the Fourier transformed wave function

$$\begin{aligned} i\hbar\partial_t\Psi(q,y,t) = &\left\{-\frac{\hbar^2}{2m^*}\left(\partial_y^2 - q^2 + \frac{2q}{l^2}y - \frac{y^2}{l^4}\right) + \frac{1}{2}m^*\Omega_0^2 y^2\right\}\Psi(q,y,t) \\ &+ \int \frac{\mathrm{d}p}{2\pi}\, V(q-p,y,t)\Psi(p,y,t)\,, \end{aligned} \tag{2.15}$$

where

$$V(q-p,y,t) = \int \mathrm{d}x\, e^{-i(q-p)x}\, V(x,y,t)\,. \tag{2.16}$$

By completing the square we can combine the effective momentum operator and the confinement potential which then allows us to write the Schrödinger equation in the form

$$\begin{aligned} i\hbar\partial_t\Psi(q,y,t) = &\left\{-\frac{\hbar^2}{2m^*}\partial_y^2 + \frac{1}{2}m^*\Omega_\omega^2(y-y_0)^2 + K(q)\right\}\Psi(q,y,t) \\ &+ \int \frac{\mathrm{d}p}{2\pi}\, V(q-p,y,t)\Psi(p,y,t)\,, \end{aligned} \tag{2.17}$$

We have collected together the terms for the magnetic field and the confinement potential to obtain an effective confinement potential[1] in a magnetic field with strength $\Omega_\omega^2 = \omega_c^2 + \Omega_0^2$ and center coordinate $y_0 = \frac{\hbar q\omega_c}{m^*\Omega_\omega^2}$. This was made possible by our careful choice of gauge. We have also defined

$$K(q) = \frac{(\hbar\Omega_0)^2}{(\hbar\Omega_\omega)^2}\frac{\hbar^2}{2m^*}q^2,$$

this term is the effective kinetic energy in the x-direction[1] in a magnetic field.
The next step is to expand the wave function in terms of eigenfunctions of a pure quantum wire[1] with a parabolic confinement in a magnetic field,

$$\Psi(p,y,t) = \sum_r \phi_r(y,p)\psi_r(p,t)\,. \tag{2.18}$$

[1] See appendix A

Using this expansion in Eq. (2.17) and exploiting the orthonormal relation of the eigenfunctions we get a quasi-1D equation for the coefficients of the expansion

$$i\hbar\partial_t\psi_n(q,t) = E_n(q)\psi_n(q,t) + \sum_r \int \frac{\mathrm{d}p}{2\pi} V_{nr}(q,p,t)\psi_r(p,t)\,, \tag{2.19}$$

where $E_n(q) = E_n + K(q) = (n+\frac{1}{2})\hbar\Omega_\omega + \frac{\hbar^2q^2}{2m^*}\frac{(\hbar\Omega_0)^2}{(\hbar\Omega_\omega)^2}$ and

$$V_{nr}(q,p,t) = \int \mathrm{d}y\, \phi_n^*(y,q)V(q-p,y,t)\phi_r(y,p)\,. \tag{2.20}$$

Equation (2.19) is a coupled non-local integral equation in momentum-space. So far its derivation has been identical to the static case and if we were to replace the time derivative on the left hand side with the total energy of the system it would be identical to the equation for the static case [3].

We know that time-dependent potentials induce inelastic scattering, furthermore we know that time-harmonic potentials induce sidebands [5]. For this reason we expand the time part of the wave function in Fourier series with frequency ω,

$$\psi_n(q,t) = e^{-i(E_0/\hbar)t}\sum_{m'=-\infty}^{m'=\infty} e^{-im'\omega t}\psi_n^{m'}(q) = \sum_{m'=-\infty}^{m'=\infty} e^{-i(E_0/\hbar+m'\omega)t}\psi_n^{m'}(q)\,, \tag{2.21}$$

and do the same for the potential,

$$\widetilde{V}_{nr}(q,p,t) = \sum_{s=-\infty}^{s=\infty} e^{-is\omega t}V_{nr}^s(q,p)\,. \tag{2.22}$$

The summation index (m) labels the sidebands caused by inelastic scattering. In Eq. (2.21) we have added a phase factor to include the incident energy of the electron. In our derivation this factor has to be put in by hand, if we however would have used Floquet theory[2] it would have come naturally. After we insert the Fourier series in Eq. (2.21) and (2.22) into Eq. (2.19) and exploit the orthonormal relations of the exponential functions we obtain an equation for the Fourier components of the wave function

$$\{E_0 + \hbar m\omega - E_n - K(q)\}\,\psi_n^m(q) = \sum_{m'r}\int \frac{\mathrm{d}p}{2\pi} V_{nr}^{m-m'}(q,p)\psi_r^{m'}(p)\,. \tag{2.23}$$

By rearranging the terms on the left hand side and defining the wave-vector (k_n^m) as

$$\frac{1}{2}\left(\frac{k_n^m}{\beta}\right)^2\frac{\hbar^2\Omega_0^2}{\hbar\Omega_\omega} = E_0 + \hbar m\omega - (n+\frac{1}{2})\hbar\Omega_\omega\,, \tag{2.24}$$

we can write Eq. (2.23) as

$$\left\{\left(\frac{k_n(E_0+\hbar m\omega)}{\beta}\right)^2 - \left(\frac{q}{\beta}\right)^2\right\}\psi_n^m(q) = \int\frac{\mathrm{d}p}{2\pi}\,\widehat{V}_{nr}^{m-m'}(q,p)\psi_r^{m'}(p)\,, \tag{2.25}$$

[2] See appendix C

where

$$\widehat{V}_{nr}^{m-m'}(q,p) = 2\frac{(\hbar\Omega_\omega)^2}{(\hbar\Omega_0)^2}\frac{\beta}{\hbar\Omega_\omega}V_{nr}^{m-m'}(q,p)\,. \tag{2.26}$$

The constant β is the reciprocal of the effective magnetic length[3] given by

$$\beta^2 = \frac{m^*\Omega_\omega}{\hbar}.$$

We can now define the Green's function for the system from Eq. (2.25)

$$\left\{\left(\frac{k_n(E_0+\hbar m\omega)}{\beta}\right)^2 - \left(\frac{q}{\beta}\right)^2\right\} G_n^m(q) = 1\,, \tag{2.27}$$

and we also define the incoming wave as

$$\left\{\left(\frac{k_n(E_0+\hbar m\omega)}{\beta}\right)^2 - \left(\frac{q}{\beta}\right)^2\right\} \psi_n^{m,0}(q) = 0\,. \tag{2.28}$$

Using Eq. (2.27) and (2.28) we can write down the Lippmann-Schwinger equation for the Fourier components of the wave function

$$\psi_n^m(q) = \psi_n^{m,0}(q) + G_n^m(q)\sum_{m'r}\int\frac{\mathrm{d}(p/\beta)}{2\pi}\,\widehat{V}_{nr}^{m-m'}(q,p)\psi_r^{m'}(p)\,. \tag{2.29}$$

2.3 Transmission Coefficient

Equation (2.29) is a coupled integral equation for the Fourier components of the wave function. If we could solve it we would be able to find the full wave function of the system by working our way backwards using Eqs. (2.21) and (2.18). However, Eq. (2.29) has to be solved numerically and attacking it directly is difficult, because in Fourier space the incoming wave is a delta function. To remedy this issue we assume an operator T, of the resolvent type such that

$$\psi = (1+GT)\psi_0\,. \tag{2.30}$$

We have written the equation in operator form to suppress the sums and integrals for clarity and have defined the operator T as

$$T = V + VGT\,, \tag{2.31}$$

this operator could be used to supply the Von Neumann series, but instead we solve here

$$T_{n'n}^{m'm}(q,p) = V_{n'n}^{m'-m} + \sum_{rs}\int\frac{\mathrm{d}k}{2\pi}V_{n'r}^{m'-s}(q,k)G_r^s(k)T_{rn}^{sm}(k,p) \tag{2.32}$$

[3] See appendix A

directly. The above equation for the T-matrix is also a coupled integral equation like Eq. (2.29), but has the advantage of being more easily solved numerically.

Now that we have an equation that we can deal with numerically[4] we want to find the full wave function of the system in terms of the T-matrix. Equation (2.30) is a relationship between the T-matrix and the Fourier components of the wave function and writing it out we get

$$\psi_{n'}^{m'}(q) = \psi_{n'}^{m',0}(q) + G_{n'}^{m'}(q) \sum_{rs} \int \frac{\mathrm{d}k}{2\pi} T_{n'r}^{m's}(q,k) \psi_r^{s,0}(k) \,. \tag{2.33}$$

By using Eqs. (2.21), (2.18) and (2.14) we can find an expression for the full wave function of the system

$$\Psi(x,y,t) = \Psi^0(x,y,t) + \sum_{n'm'} \int \frac{\mathrm{d}q}{2\pi} \phi_{n'}(q,y) e^{-i(E_0/\hbar + m'\omega)t} e^{iqx} G_{n'}^{m'}(q) T_{n'n}^{m'0}(q,k_n^0) \,. \tag{2.34}$$

The incoming wave ($\Psi^0(x,y,t)$) has been chosen to enter the system in subband n and sideband $m = 0$. To find the transmission coefficient we need to calculate the integral in Eq. (2.34). The Green's function in the integral gives two poles that we must handle using complex integration. We start by rewriting the integral as

$$\Psi(x,y,t) = \Psi^0(x,y,t) - \sum_{n'm'} \int \frac{\mathrm{d}q}{2\pi} \frac{e^{iqx}}{(q-k_{n'}^{m'})(q+k_{n'}^{m'})} \phi_{n'}(q,y) e^{-i(E_0/\hbar + m'\omega)t} T_{n'n}^{m'0}(q,k_n^0) \,. \tag{2.35}$$

Then by taking only the contribution of the pole that gives a wave travelling in the $+x$-direction we obtain by using residue integration

$$\Psi(x,y,t) = \Psi^0(x,y,t) - \sum_{n'm'} \frac{1}{2k_{n'}^{m'}} e^{ik_{n'}^{m'}x} \phi_{n'}(k_{n'}^{m'},y) e^{-i(E_0/\hbar + m'\omega)t} T_{n'n}^{m'0}(k_{n'}^{m'},k_n^0) \,, \tag{2.36}$$

and from this expression we see that the transmission coefficient is given by

$$t_{n'n}^{m'0} = \delta_{n'n}\delta_{m'0} - \frac{i}{2k_{n'}^{m'}} T_{n'n}^{m'0}(k_{n'}^{m'},k_n^0) \,. \tag{2.37}$$

When the T-matrix has been calculated numerically we can use Eq. (2.10) to find the conductance of the system.

2.4 The Potential

We have been able to develop a whole model for transport through a quantum wire without saying much about the form of the potential. We have only assumed that it depends on (x, y) and t. There are some interesting and important consequences if the

[4] Appendix D details the preparation for the numerical calculations.

potential is independent of one or more of these variables. An examination of Eq. (2.20) is worthwhile because it takes on the role of a coupling constant in Eq. (2.19) that couples together different subbands. This equation gives selection rules for jumps between different subbands. An interesting case arises when the potential is independent of y as then the potential can be taken outside the integral and the orthogonality relation of the basis forbids jumps between different subbands. Therefore, in the case of potential that is homogeneous in the y-direction inter-subband transitions are forbidden and only intra-subband transitions are allowed. The details of the calculations of the integral in equation (2.20) can be seen in appendix B.

Equation (2.19) is also interesting because the potential is no longer local. In other words the interactions at one point depend on the value of the potential at all points in space. This is interesting because we began with a potential that was local, but the magnetic field with its Lorentz force have transformed the action of the potential into the non-local form. Another interesting thing is that the sum in the equation runs over all subbands, not just the propagating ones and thus evanescent mode cannot be neglected [2].

We would now like to define the potential and examine what consequences its form has on the system. Let us consider the potential

$$V(x,y,t) = V_s(x,y) + V_t(x,y)\cos(\omega t)\,, \tag{2.38}$$

i.e. a static potential plus a part that fluctuates harmonically in time with the frequency ω. By use of Eqs. (2.20) and (2.16) we have

$$V_{n'n}(q,p,t) = V_{s,n'n}(q,p) + V_{t,n'n}(q,p)\cos(\omega t)\,. \tag{2.39}$$

Expanding the potential in a Fourier series with the same fundamental frequency as is done with the potential in Eq. (2.22) gives selection rules between the sidebands,

$$V^m_{n'n}(q,p) = V_{s,n'n}(q,p)\delta_{m,0} + \frac{1}{2}V_{t,n'n}(\delta_{m,-1} + \delta_{m,1})\,. \tag{2.40}$$

Inserting the above equation into Eq. (2.32) for the T-matrix yields

$$\begin{aligned} T^{m'm}_{n'n}(q,p) &= V_{s,n'n}(q,p)\delta_{m'-m,0} + \frac{1}{2}V_{t,n'n}(q,p)(\delta_{m'-m,-1} + \delta_{m'-m,1}) \\ &+ \sum_r \int \frac{\mathrm{d}k}{2\pi} V_{s,n'r}(q,k) G^{m'}_r(k) T^{m'm}_{rn}(k,p) \\ &+ \frac{1}{2}\sum_r \int \frac{\mathrm{d}k}{2\pi} V_{t,n'r}(q,k) G^{m'+1}_r(k) T^{(m'+1)\,m}_{rn}(k,p) \\ &+ \frac{1}{2}\sum_r \int \frac{\mathrm{d}k}{2\pi} V_{t,n'r}(q,k) G^{m'-1}_r(k) T^{(m'-1)\,m}_{rn}(k,p)\,. \end{aligned} \tag{2.41}$$

The equation for the T-matrix couples together adjacent sidebands because of the harmonic term in the potential and intra-sideband transitions occur because of the static part of the potential.

CHAPTER 3

Numerical Results

The previous chapter discussed the theoretical framework for a quantum wire with a potential that is periodic in time. This framework laid down the groundwork for numerical calculations of such systems. Equation (2.41) was the main result and in appendix D it is shown how it is prepared for numerical evaluation. The main focus of this thesis will be to investigate transport through Quantum Point Contacts (QPCs). Such systems are expected to have a rich structure in the conductance for a variety of reasons.

In the numerical calculations the wire is taken to be that in a high-mobility ($\mu_e \sim 10^4 - 10^6\,\mathrm{cm}^2/\mathrm{Vs}$) GaAs/$Ga_{1-x}Al_xAs$ heterostructure, such as the one in Fig. 1.1. The electron density is $n_s \sim 4 \times 10^{11}\,\mathrm{cm}^{-2}$ with an effective electron mass of $m^* = 0.067 m_e$. The confinement potential is fixed at $\hbar\Omega_0 = 1.0\,\mathrm{meV}$. Energies have been scaled using $\hbar\Omega_\omega$ the effective strength of the confinement potential in a magnetic field, except the strength of the potentials which are fixed in meV and can be compared with the relevant energy scales in Tbl. I. Lengths have been scaled using β, the reciprocal of the effective magnetic length. Length parameters for the potentials have been defined in units of β_0^{-1} ($\approx 33.72\,\mathrm{nm}$) the effective length at zero magnetic field.

3.1 Simple Time-Periodic Potentials

Simple time-harmonic potentials and their effects on the conductance have been investigated before [10–12]. These investigation have been limited by the use of delta functions or potentials with sharp edges. Presented here are calculations for a potential that varies smoothly over the wire. The fundamental results should be the same but effects from artificial sharp boundaries should not be present. These calculations should be closer to

experimental results since potentials are usually created electrostatically in experiments and hence vary smoothly.

3.1.1 Time-Harmonic Gaussian

Starting with a simple smooth time-harmonic Gaussian with the form

$$V(x,y,t) = V_0 e^{-\alpha_x x^2 - \alpha_y y^2} \cos(\omega t)\,,$$

where the parameters are

$$V_0 = 0.8\,\text{meV}, \quad \alpha_x = 3.5\beta_0^2, \quad \alpha_y = 3.5\beta_0^2, \quad \omega/\Omega_\omega = 0.17\,.$$

In Fig. 3.2 the conductance of a wire with the above potential embedded is compared with an ideal wire and a wire with a static attractive Gaussian with the same parameters. It can be seen in the figure that the conductance of the time-modulated potential is higher

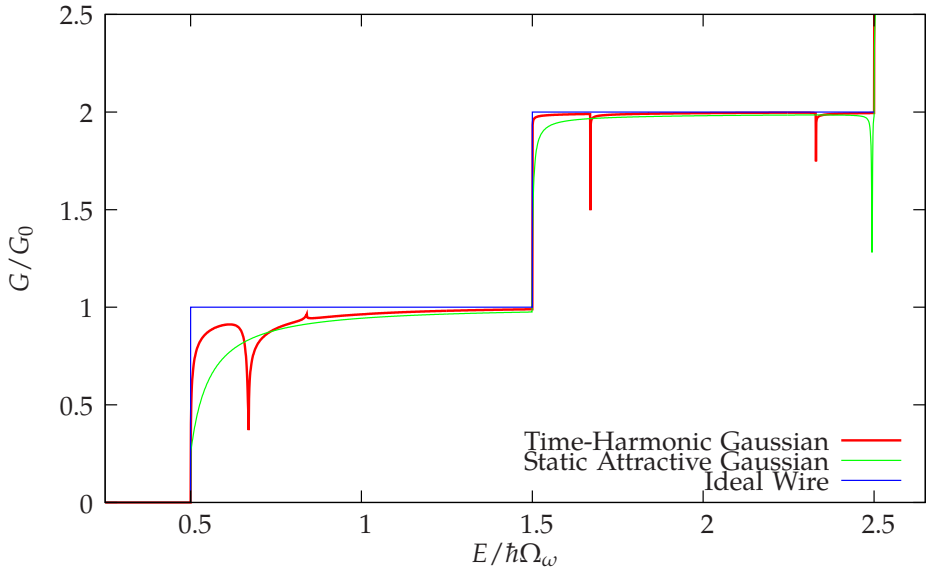

FIG. 3.1: The conductance of the time-harmonic Gaussian-shaped potential compared to a static attractive Gaussian potential with the same parameters without a magnetic field.

than in the static case for most values of the incident energy. The time-averaged height of an oscillating barrier is lower than the height of a static barrier, which consequently allows more transmission to occur. The dip seen in second subband in the conductance of the attractive static Gaussian is not observed in the time-dependant case. This is because in the time-dependent case the Gaussian fluctuates between being attractive (well) and repulsive (hill).

A new feature seen in the oscillating case are dips and peaks in the conductance. These dip and peak structures appear just before the opening of a new conduction channel and

are of a similar nature to the dip seen in the second subband for the static barrier [10]. The dips and peaks occur at integer multiples of ω away from a subband edge as can be seen in Fig. 3.2. At these energies the electrons can make inelastic transitions to a quasi-bound state at the subband edge similar to the case of the attractive static barrier [1].

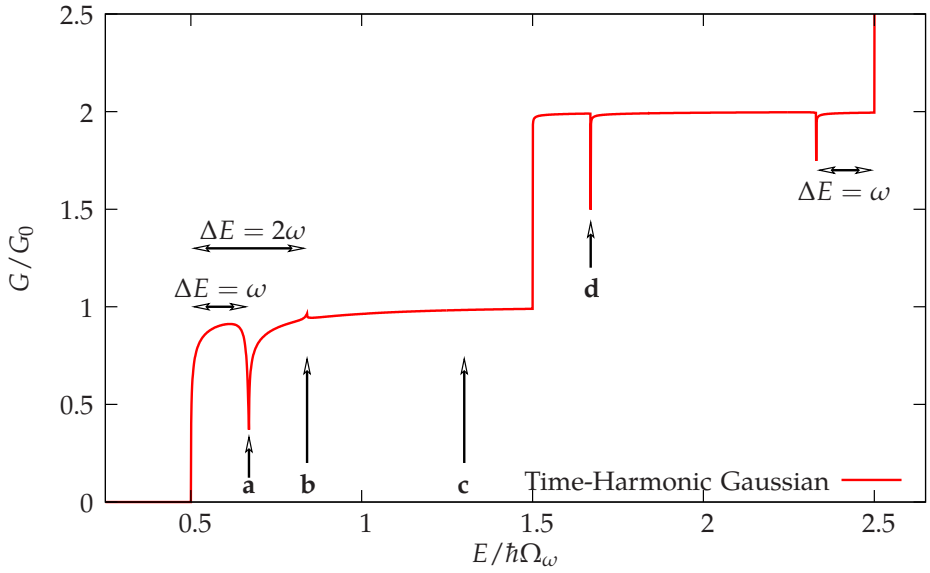

FIG. 3.2: The conductance of the time-harmonic Gaussian potential without a magnetic field.

In Fig. 3.3 the probability density at the energies indicated in Fig. 3.2 can be seen. The beating pattern seen in the figures is due to a summation of waves with different energies (phases). This can be seen most clearly at the points closest to the opening of the new conduction channels such as in Fig. 3.3a, 3.3b and 3.3d because at these points inelastic scattering is expected. Further away from the opening of conduction channels inelastic scattering is expected to become less frequent and conductance should approach the static case. The probability density seen in Fig. 3.3c at a point far away from the opening of an inelastic conduction channel looks similar to that seen in the static case [1].

Figure 3.4 shows the conductance in a magnetic field. The conductance is higher in a magnetic field because the Lorentz force pushes the electrons into the wall away from the Gaussian potential in the middle of the wire. An inset in Fig. 3.4 shows an enlargement of the conductance at the second peak-dip structure. The magnetic field turns the peak there into a dip and at even higher magnetic fields it disappears.

The first dip can also by reversed and turned into a peak by making the Gaussian-shaped potential very wide in the x-direction. In Fig. 3.5 the conductance of the time-harmonic Gaussian is compared to a time-harmonic Gaussian that has been made very wide in the x-direction, i.e. $\alpha_x = 0.1$ while other parameters are kept the same. When potential is

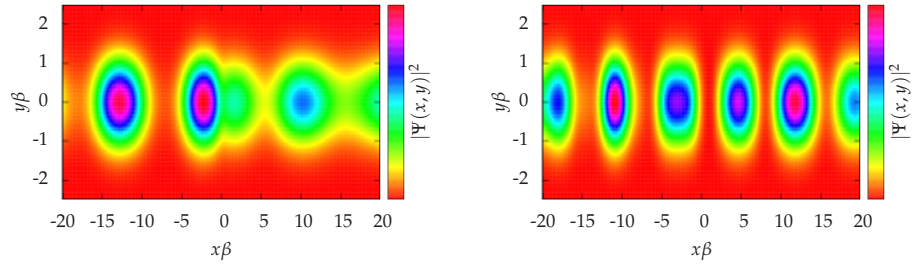

(a) Point **a** ($E/\hbar\Omega_\omega = 0.67$, $n = 0$).

(b) Point **b** ($E/\hbar\Omega_\omega = 0.84$, $n = 0$).

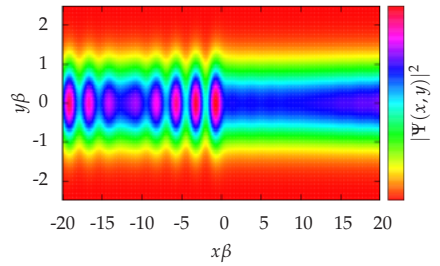

(c) Point **c** ($E/\hbar\Omega_\omega = 1.3$, $n = 0$).

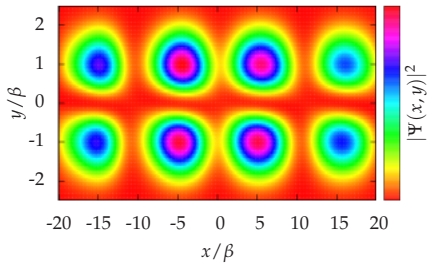

(d) Point **d** ($E/\hbar\Omega_\omega = 1.67$, $n = 1$).

FIG. 3.3: The probability density for the simple time-harmonic Gaussian potential at the energies indicated in Fig. 3.2.

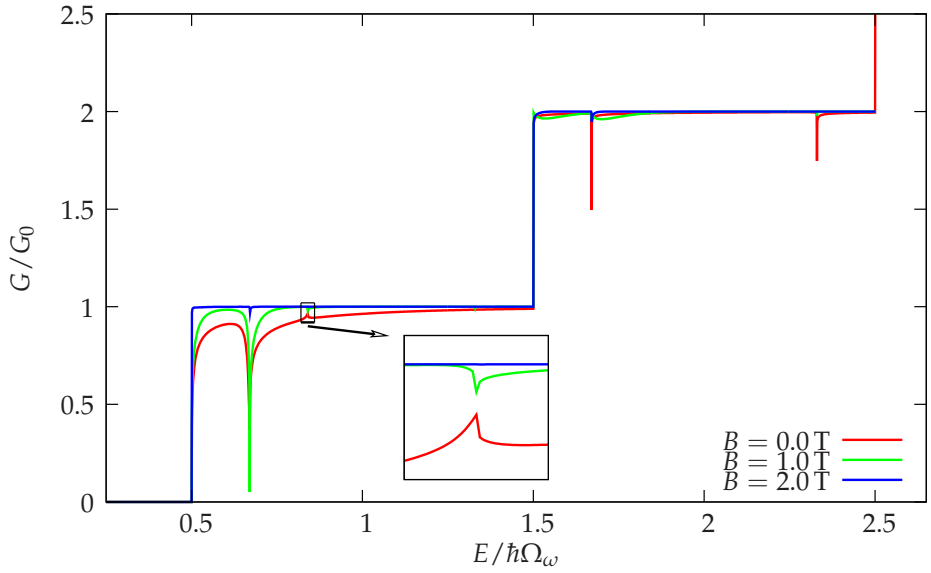

FIG. 3.4: The conductance of the time-harmonic Gaussian in a magnetic field.

made very wide it becomes easier to excite electrons out of the QBS. The dip therefore turns into a peak because of the opening of a new conduction channel.

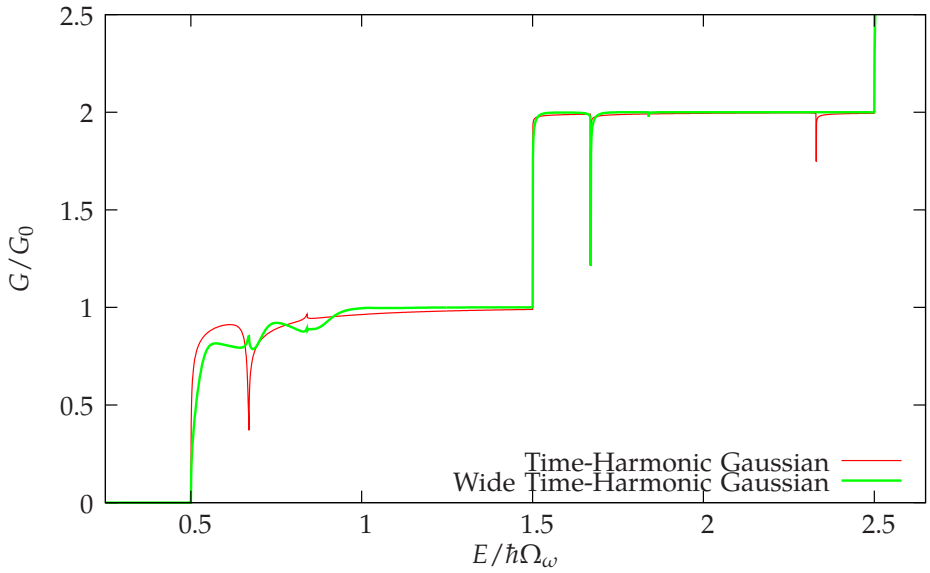

FIG. 3.5: The conductance of the time-harmonic Gaussian compared with the conductance of a narrow time-harmonic Gaussian.

3.1.2 Time-Harmonic Well

Another system of interest is a well with a bottom that oscillates in time. The potential has the form

$$V(x,y,t) = V_s e^{-\alpha_x x^2 - \alpha_y y^2} + V_t e^{-\gamma_x x^2 - \gamma_y y^2} \cos(\omega t)\,,$$

where

$$V_s = -0.4\,\text{meV}, \quad \alpha_x = 3.5\beta_0^2, \quad \alpha_y = 0.5\beta_0^2\,,$$

$$V_t = 0.3\,\text{meV}, \quad \gamma_x = 10.0\beta_0^2, \quad \gamma_y = 10.0\beta_0^2, \quad \omega/\Omega_\omega = 0.17\,.$$

A cross-section of this potential at its maximum and minimum can be seen in Fig. 3.6 and in Fig. 3.7 the conductance of this system is shown. The most noticeable feature in

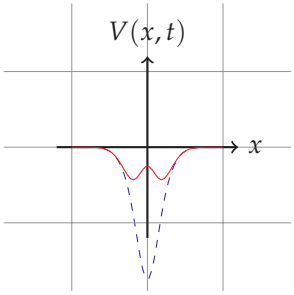

FIG. 3.6: A cross-section of the time-harmonic well at its maximum (dashed) and minimum (solid) amplitude.

the conductance is the Fano resonance in the first subband. The probability density at the point marked **a** ($E/\hbar\Omega_\omega = 0.5289$) in Fig. 3.7 can be seen in Fig. 3.8, and Fig. 3.9 shows the probability density at the point marked **b** ($E/\hbar\Omega_\omega = 0.5299$). The evolution of the probability density is shown over approximately one period, taken at equally spaced intervals in time. The probability density in Fig. 3.8 does not change much over time. The electron seems to be stuck in the well and the system has low conductance. The opposite is seen in Fig. 3.9, the electron seems to fall into the well (Fig. 3.9d), stay there for a short period (Fig. 3.9a) and then leave (Fig. 3.9b) and a new one enters the well (Fig. 3.9d). This process is due to inelastic scattering. The electron loses energy when it falls into the well and gains energy when it climbs out again.

The dip at the end of the second subband (marked **d** in Fig. 3.7) is also interesting. This dip is due to backscattering by a quasi-bound state originating from an evanescent mode, i.e. a coupling of the first and the third subbands. This dip also appears in the static case [1] and can be seen in Fig. 3.7 for the static attractive Gaussian. A snapshot of the probability density at this dip can be seen in Fig. 3.10 along with the probability density at the dip

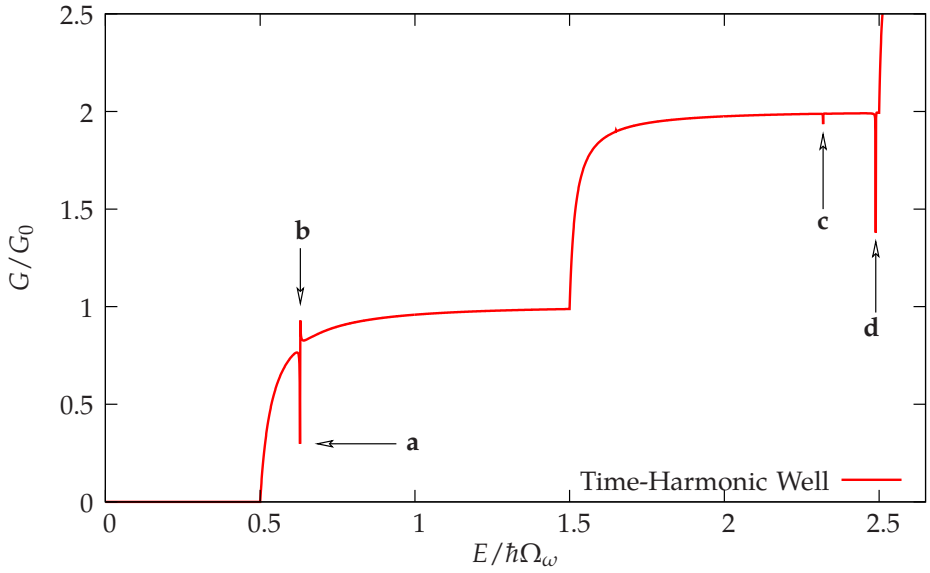

FIG. 3.7: The conductance of the well with an oscillating bottom without a magnetic field.

marked **c** in Fig. 3.7, which is located approximately ω away from the nearest subband edge. As mentioned in the previous section these dips are of a similar nature and the probability densities are quite similar, i.e. they both show coupling to an evanescent mode in the third subband. The main difference between the two dips is that the dip marked **c** is due to inelastic scattering while the dip marked **d** is the result of elastic scattering.

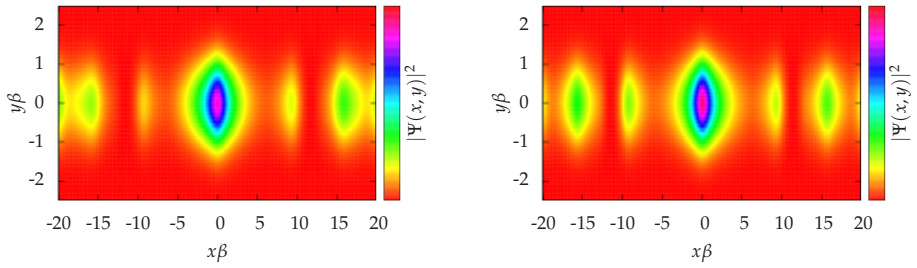

(a) $t\Omega_\omega = 0.00$ ($t = 0.00\,\mathrm{ps}$).

(b) $t\Omega_\omega = 8.87$ ($t = 5.84\,\mathrm{ps}$).

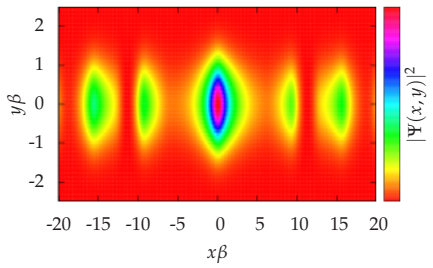

(c) $t\Omega_\omega = 18.11$ ($t = 11.92\,\mathrm{ps}$).

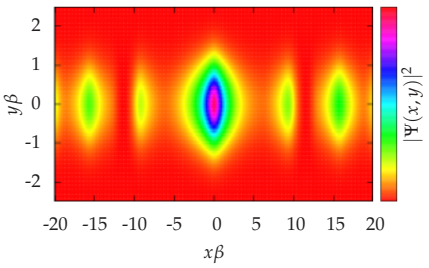

(d) $t\Omega_\omega = 27.35$ ($t = 18.00\,\mathrm{ps}$).

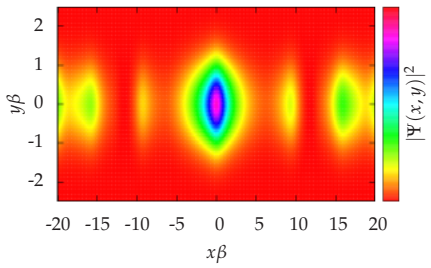

(e) $t\Omega_\omega = 36.59$ ($t = 24.08\,\mathrm{ps}$).

FIG. 3.8: The probability density over approximately one period at the point marked **a** in Fig. 3.7.

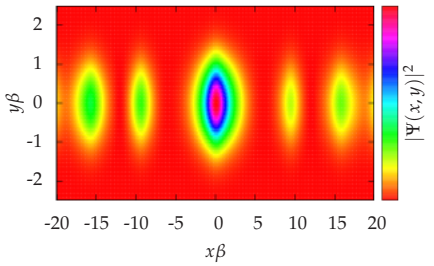

(a) $t\Omega_\omega = 0.0$ ($t = 0.00\,\mathrm{ps}$).

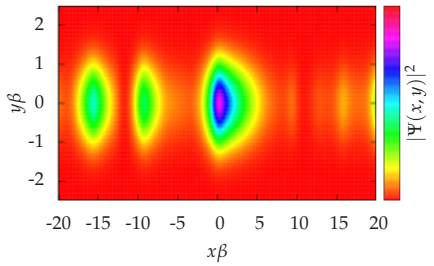

(b) $t\Omega_\omega = 8.87$ ($t = 5.84\,\mathrm{ps}$).

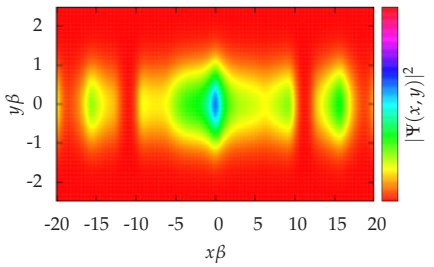

(c) $t\Omega_\omega = 18.11$ ($t = 11.92\,\mathrm{ps}$).

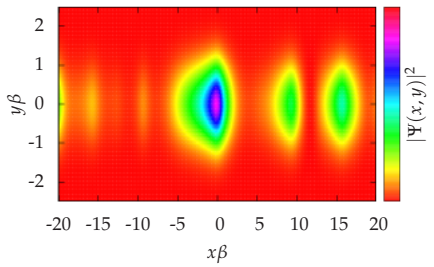

(d) $t\Omega_\omega = 27.35$ ($t = 18.00\,\mathrm{ps}$).

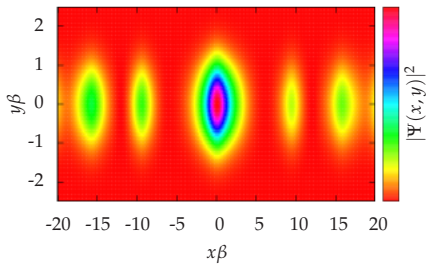

(e) $t\Omega_\omega = 36.59$ ($t = 24.08\,\mathrm{ps}$).

FIG. 3.9: The probability density over approximately one period at the point marked **b** in Fig. 3.7.

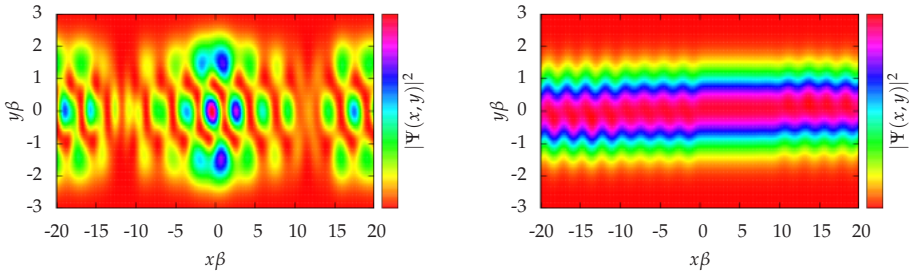

(a) Point **c** ($E/\hbar\Omega_\omega = 2.319$, $n = 0$).

(b) Point **c** ($E/\hbar\Omega_\omega = 2.319$, $n = 1$).

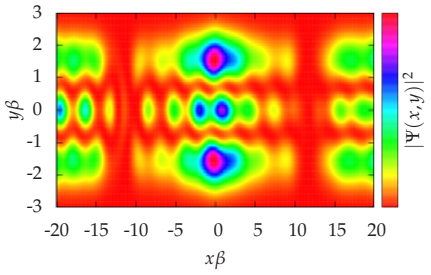

(c) Point **d** ($E/\hbar\Omega_\omega = 2.489$, $n = 0$).

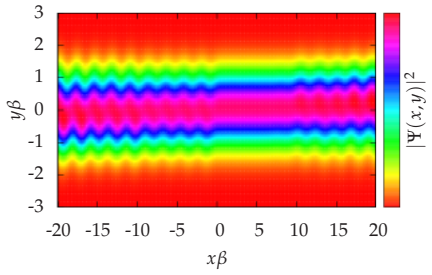

(d) Point **d** ($E/\hbar\Omega_\omega = 2.489$, $n = 1$).

FIG. 3.10: Probability density at the points marked **c** and **d** in Fig. 3.7.

3.2 Quantum Point Contact

Quantum Point Contacts (QPCs) have received much attention since it was discovered that their conductance is quantised [13]. A QPC is essentially a constriction and a lot of attention has been given to the step that forms in the bottleneck of the constriction [14]. This step is indeed important when there is no magnetic field and the incident wave is in the first subband, because then the wave is centred and scatters mostly on the step. However, when the incident wave is no longer in the first subband or is in a magnetic field extended parts of the geometry will become more important. Presented here are calculations for processes in the first two subbands in a quantum wire with and without a magnetic field. In the numerical calculations the first eight subbands were taken into account.

Starting with a static QPC made up of two Gaussian potentials,

$$V(x,y) = V_1 e^{-\alpha_x x^2 - \alpha_y (y-y_1)^2} + V_2 e^{-\gamma_x x^2 - \gamma_y (y-y_2)^2}\,, \tag{3.1}$$

with the parameters,

$$V_1 = 6.5\,\text{meV}, \quad \alpha_x = 0.5\beta_0^2, \quad \alpha_y = 0.3\beta_0^2, \quad y_1 = \;\; 3\beta_0,$$

$$V_2 = 6.5\,\text{meV}, \quad \gamma_x = 0.5\beta_0^2, \quad \gamma_y = 0.3\beta_0^2, \quad y_2 = -3\beta_0\,.$$

This system can be seen in Fig. 3.11. The minimum height of the step in the middle of the

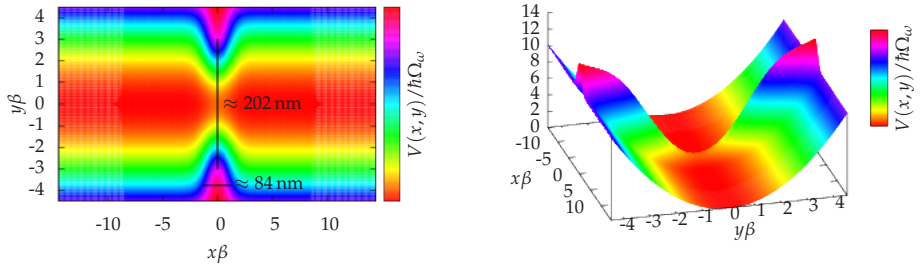

(a) Contour plot. (b) 3D plot.

FIG. 3.11: A plot of the single Quantum Point Contact (QPC) embedded in a wire with a parabolic confinement.

Gaussian peaks is about 0.9 meV. The conductance without a magnetic field is presented in Fig. 3.12. The conductance shows quantised steps that are lower than the quantised steps of an ideal wire due to scattering from the constriction. The conductance of the QPC also has a smooth opening due to tunnelling trough the smoothly varying potential and at higher energies the conductance starts to become linear.

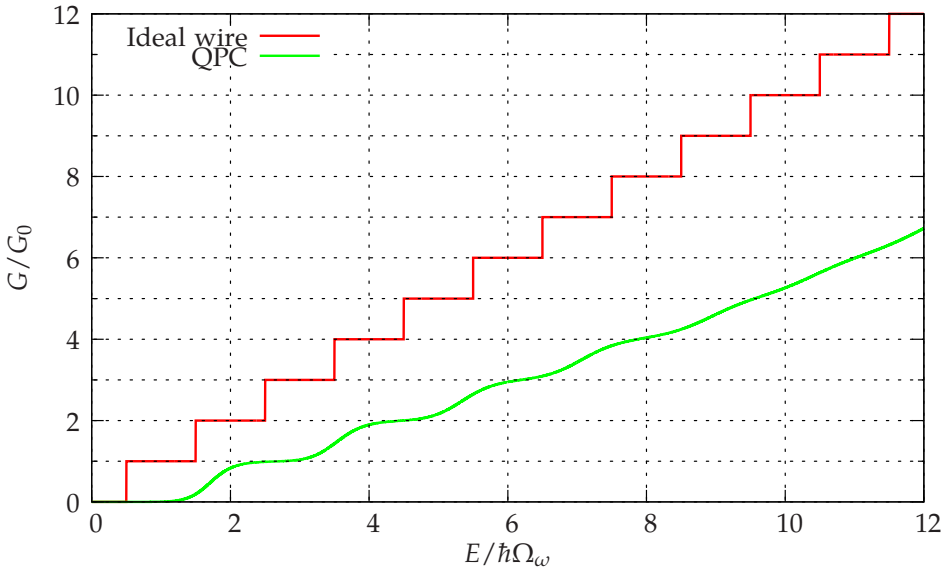

FIG. 3.12: The conductance through the QPC without a magnetic field.

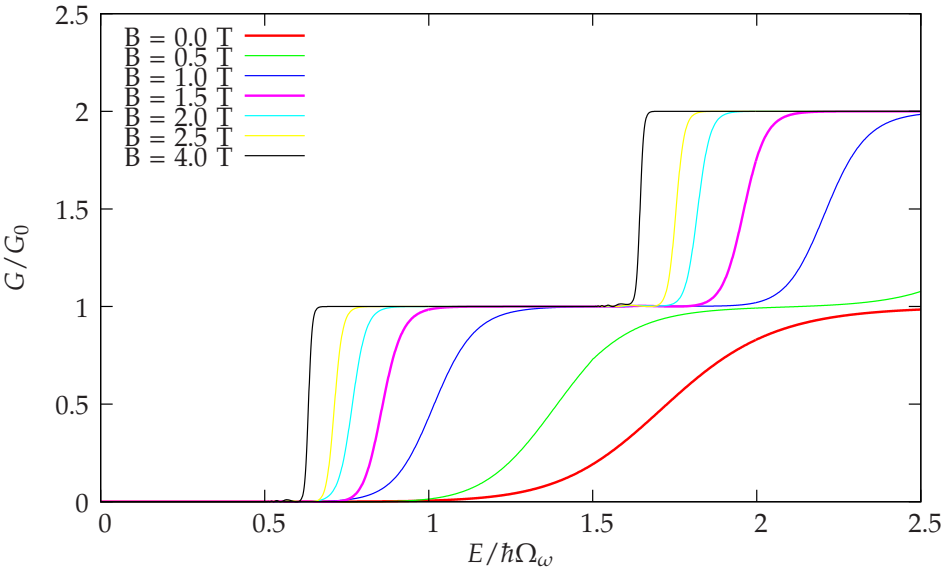

FIG. 3.13: Evolution of the conductance through the QPC in a magnetic field.

B	l [nm]	$1/\beta$ [nm]	$l\beta$	$\hbar\omega_c$ [meV]	$\hbar\Omega_\omega$ [meV]
0.0	∞	33.72 nm	∞	0.0 meV	1.0 meV
0.5	36.29 nm	29.33 nm	1.24	0.86 meV	1.32 meV
1.0	25.66 nm	23.87 nm	1.07	1.72 meV	2.00 meV
1.5	20.95 nm	20.23 nm	1.04	2.59 meV	2.78 meV
2.0	18.14 nm	17.78 nm	1.02	3.46 meV	3.60 meV

Table I: Comparison of the magnetic length scales.

Figure 3.13 shows the conductance of the QPC in a magnetic field. Plateaus begin to form in high magnetic fields and the conductance starts to approach the step like conductance of an ideal wire. In Fig. 3.14 the probability density at a fixed energy ($E/\hbar\Omega_\omega = 1.32$) can

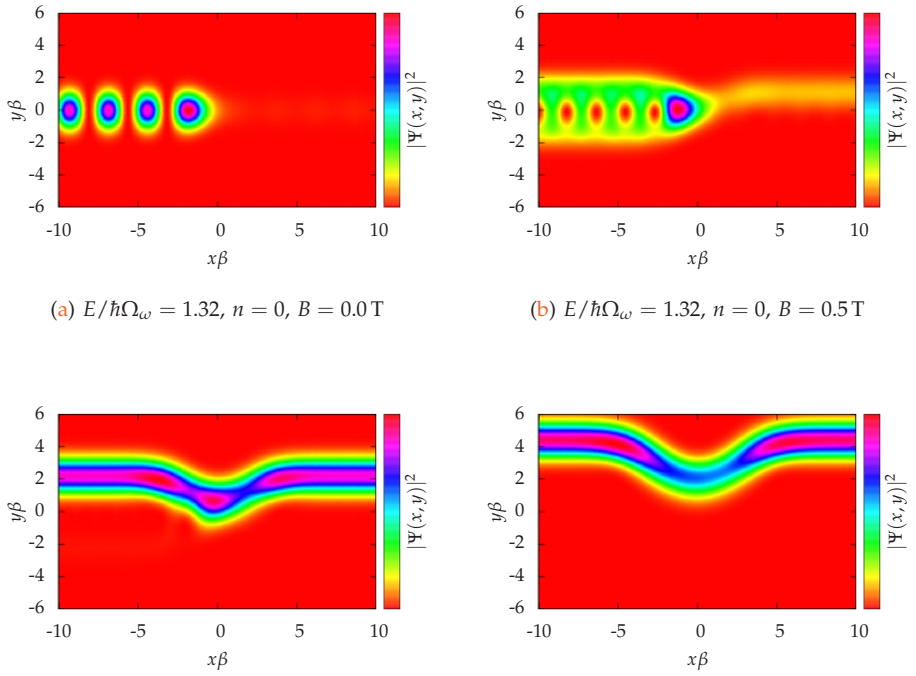

(a) $E/\hbar\Omega_\omega = 1.32$, $n = 0$, $B = 0.0\,\mathrm{T}$

(b) $E/\hbar\Omega_\omega = 1.32$, $n = 0$, $B = 0.5\,\mathrm{T}$

(c) $E/\hbar\Omega_\omega = 1.32$, $n = 0$, $B = 1.0\,\mathrm{T}$

(d) $E/\hbar\Omega_\omega = 1.32$, $n = 0$, $B = 2.0\,\mathrm{T}$

FIG. 3.14: Probability density in the QPC at a fixed energies for different values of the magnetic field.

be seen for a few values of the magnetic field. At low magnetic fields (Fig. 3.14a and 3.14b) we can clearly see interference due to scattering in the probability density, but at higher values (Fig. 3.14c and 3.14d) the interference disappears and we have an edge state. In those states the electrons follow the equipotential lines of the potential. Table I shows a comparison of the different length scales present in a magnetic field. As the magnetic field increases the effective length scales become smaller and the potential becomes smooth on the scale of the magnetic length. Backscatterings also become less frequent due less overlapping of the edge states at the two edges as the magnetic length decreases.

3.3 Double Quantum Point Contact

A double QPC is made up of two QPCs in series. Such a double QPC system forms a cavity between the QPCs that can trap electron in quasi-bound states (QBS). This cavity is also important in magnetic fields as electrons can execute a cyclotron motion inside it. A device such as this could be used as an interferometer [15–17].

3.3.1 Static Double Quantum Point Contact

A static double QPC has the following form

$$\begin{aligned} V(x,y) &= V_1 e^{-\alpha_x (x-x_1)^2 - \alpha_y (y-y_1)^2} + V_2 e^{-\gamma_x (x-x_2)^2 - \gamma_y (y-y_2)^2} \\ &+ V_3 e^{-\eta_x (x-x_3)^2 - \eta_y (y-y_3)^2} + V_4 e^{-\nu_x (x-x_4)^2 - \nu_y (y-y_4)^2}, \end{aligned} \tag{3.2}$$

with the parameters,

$$\begin{aligned} V_1 &= 6.5\,\text{meV}, \quad \alpha_x = 0.5\beta_0^2, \quad \alpha_y = 0.3\beta_0^2, \quad x_1 = 8\beta_0, \quad y_1 = -3\beta_0, \\ V_2 &= 6.5\,\text{meV}, \quad \gamma_x = 0.5\beta_0^2, \quad \gamma_y = 0.3\beta_0^2, \quad x_2 = 8\beta_0, \quad y_2 = 3\beta_0, \\ V_3 &= 6.5\,\text{meV}, \quad \eta_x = 0.5\beta_0^2, \quad \eta_y = 0.3\beta_0^2, \quad x_3 = -8\beta_0, \quad y_3 = -3\beta_0, \\ V_4 &= 6.5\,\text{meV}, \quad \nu_x = 0.5\beta_0^2, \quad \nu_y = 0.3\beta_0^2, \quad x_4 = -8\beta_0, \quad y_4 = 3\beta_0\,. \end{aligned}$$

In Fig. 3.15 we see this system embedded in a wire. The potentials have been placed

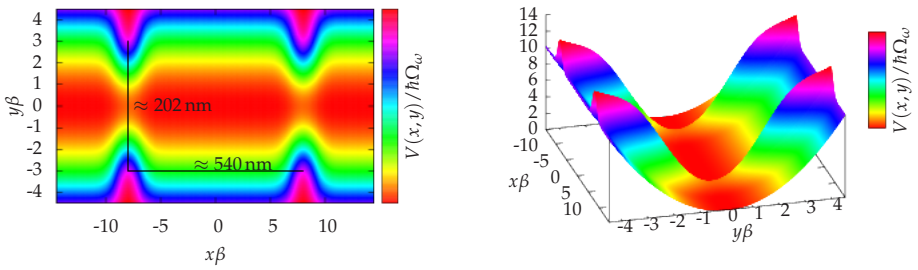

(a) Contour plot. (b) 3D plot.

FIG. 3.15: A plot of the double QPC embedded in a wire with a parabolic confinement.

into the walls of the wire in such a way that electrons cannot pass between the walls and the Gaussian peaks, but must go over the step between the peaks which has a minimum height of 0.9 meV in the center. This value can be compared with the relevant energy scales in Tbl. I. The conductance through the system is presented in Fig. 3.16 without a magnetic field. As expected the conductance shows a lot more structure than the single QPC, which

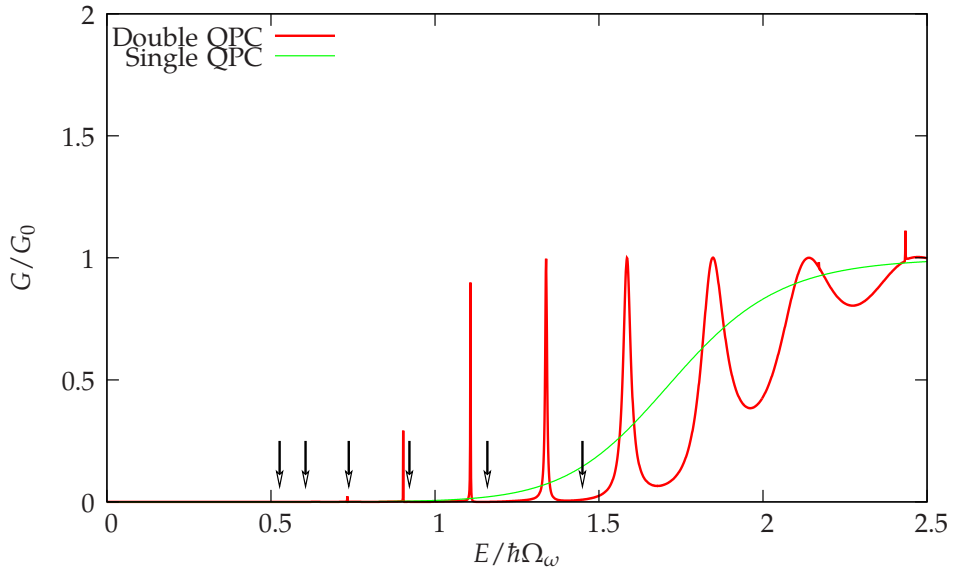

FIG. 3.16: The resonances in the conductance of the double QPC compared with the bound states of a finite wire (**black arrows**) calculated with Eq. (A.18) ($L\beta = 13.68$). Also shown for comparison is the conductance of the single QPC.

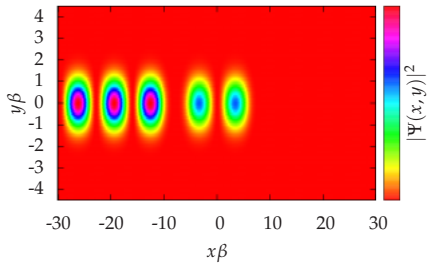

(a) Point **a** ($E/\hbar\Omega_\omega = 0.606$).

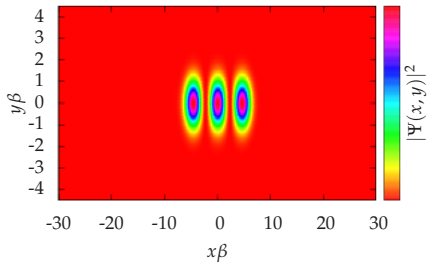

(b) Point **b** ($E/\hbar\Omega_\omega = 0.73315$).

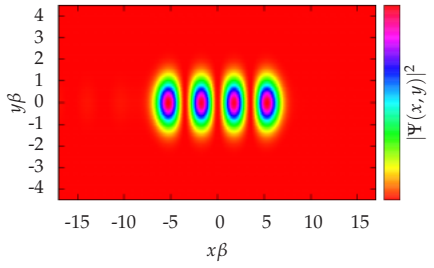

(c) Point **c** ($E/\hbar\Omega_\omega = 0.903$).

FIG. 3.17: Probability density for the resonances marked in Fig. 3.19a.

is shown for comparison. The resonances seen are quasi-bound states (QBS) inside the cavity. This is confirmed by comparing the resonances with the calculated bound states of an ideal finite wire (Eq. A.18) and also by examining the probability density at the resonances, which are shown in Fig. 3.17. The bounds states calculated for a finite ideal wire match the quasi-bound states in the wire at low energies but not at higher ones. This was to be expected as the potential is smooth but not a hard wall as was assumed in the case of the finite wire. The probability density for the second resonance is shown in Fig. 3.17a, which shows two peaks inside the cavity. The wavelength can be calculated by using the relation $\lambda = 2\pi/|k|$ and Eq. (2.24). The distance between the two peaks is about $L\beta = 6.80$ which compared with the wavelength $\lambda\beta = 13.65$ at $E/\hbar\Omega_\omega = 0.606$ gives a ratio of $\lambda\beta/L\beta = 2.01$. Similarly the probability density for the third and fourth resonances which are shown in Figs. 3.17b and 3.17c show three and four peaks inside the cavity respectively. The distances between those peaks and the corresponding wavelength also give a ratio of $\lambda\beta/L\beta \approx 2.0$. In Fig. 3.18 the probability density at the resonances is compared with the probability density in a finite wire with hard walls. A double QPC has also been placed inside the finite wire with the same parameters. The main difference between the two system is that the finite wire is a closed system with a discrete spectrum, while the other is an open system with an continuous spectrum. The results from the two systems are quite similar. The probability density of the finite wire is symmetrical about the x-axis, but in the open system the symmetry is broken due to the incoming and outgoing waves causing interference. The calculations for the finite wire were done by Prof. Viðar Guðmundsson [18] at the Science Institute of the University of Iceland.

Figure 3.19 shows the conductance of the double QPC in a magnetic field ranging from 0.0 T to 2.0 T and the conductance of the single QPC is shown for comparison. The presence of the second QPC does not lower the conductance significantly compared with the single QPC but only adds on the resonances from the quasi-bound states and the interference from the cyclotron motion of the electrons inside the cavity.

In Fig. 3.22 the conductance is shown as a function of the magnetic field. The energy has been fixed at the points shown in Fig. 3.21. At higher energies (Figs. 3.22b, 3.22c and 3.22d) the conductance is periodic as a function of the magnetic field, which is a clear sign of AB oscillations [19, 20] in the system. The area enclosed by the circular path taken by the electrons is related to the periodicity of the AB oscillations via the relation

$$A = \frac{2\pi}{\Delta B}\frac{\hbar}{e}. \tag{3.3}$$

The period of the large oscillations in Fig. 3.22c is approximately $\Delta B = 0.5\,\mathrm{T}$ and $\Delta B = 0.02\,\mathrm{T}$ for the smaller oscillations seen in the inset of the figure. The larger oscillations thus

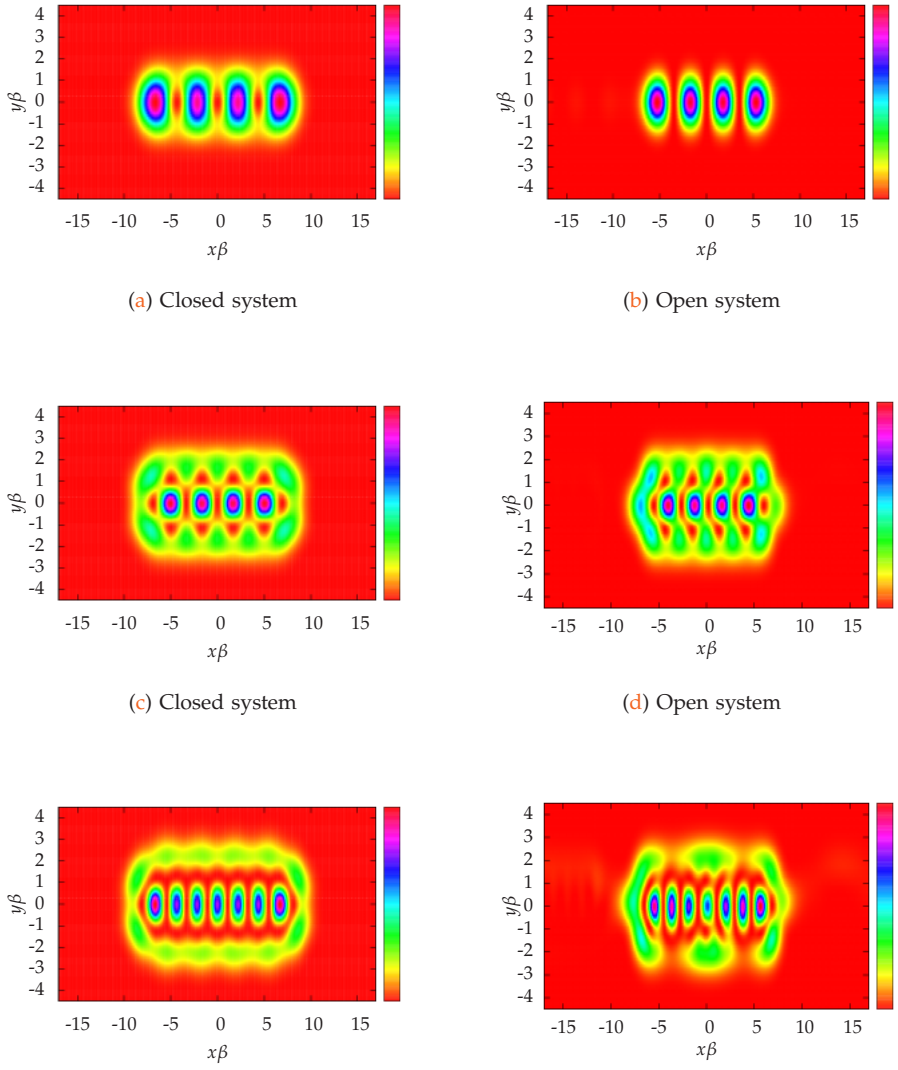

(a) Closed system

(b) Open system

(c) Closed system

(d) Open system

(e) Closed system

(f) Open system

FIG. 3.18: Comparison of the QBS in a closed and an open system.

give an area of $A \approx 8100\,\mathrm{nm}^2$ which corresponds to a box with length $l \approx 2.6/\beta_0$. This box fits fairly well inside the constriction of one of the QPCs as can be seen in Fig. 3.23a. The smaller oscillations give an area of $A \approx 207000\,\mathrm{nm}^2$, which fits fairly well within the cavity if we assume a box of size $A \approx 2.5/\beta_0 \times 7.25/\beta_0$ as in Fig. 3.23b. Figure 3.24 shows the paths taken by electrons causing the AB oscillations in the double QPC. An incoming wave is partially reflected and transmitted at the first QPC and also on the second QPC. This creates the circular path taken by the electrons inside the cavity (red area), which cause the smaller AB oscillations. When the wave that reflects of the second

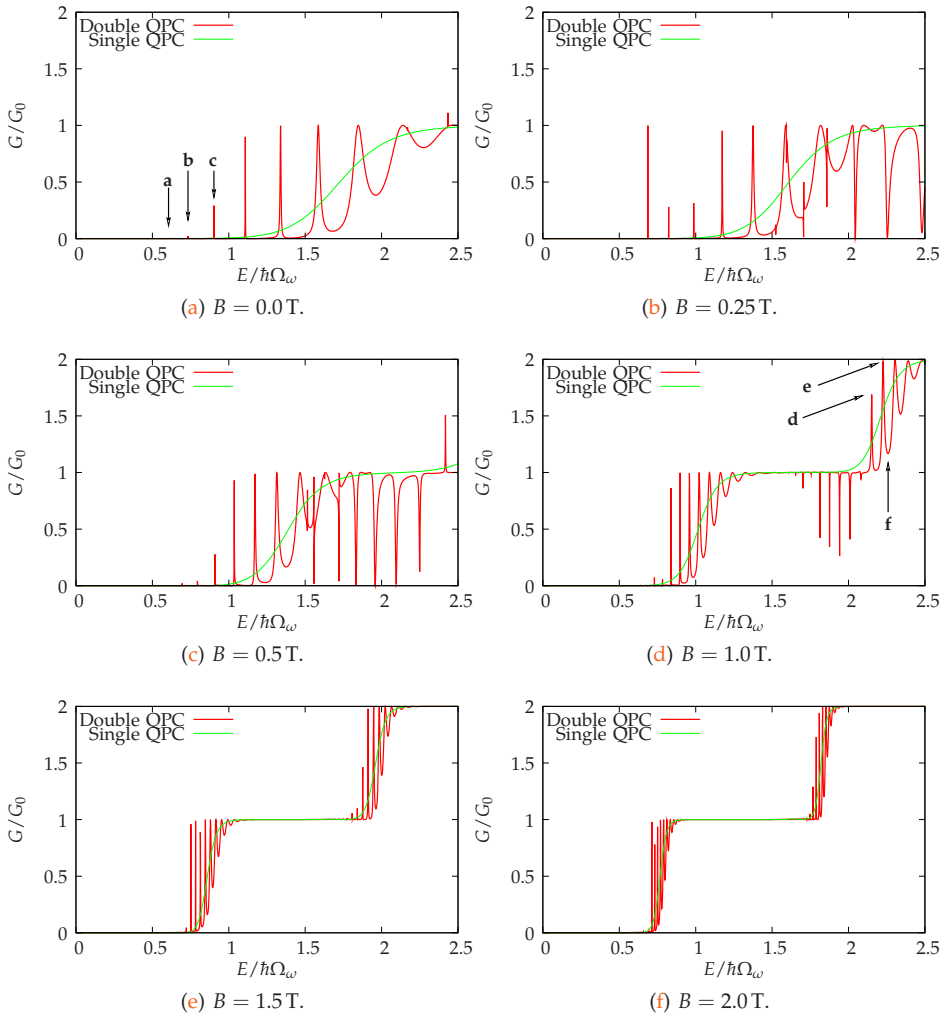

(a) $B = 0.0\,\mathrm{T}$. (b) $B = 0.25\,\mathrm{T}$.

(c) $B = 0.5\,\mathrm{T}$. (d) $B = 1.0\,\mathrm{T}$.

(e) $B = 1.5\,\mathrm{T}$. (f) $B = 2.0\,\mathrm{T}$.

FIG. 3.19: Evolution of the conductance through the double QPC in a magnetic field.

QPC enters the constriction of the first QPC electrons can interfere with the incoming wave by tunnelling from an edge state to another one on the opposite side in the constriction (blue area), which causes the larger AB oscillations. These effects have been measured experimentally in a single QPC [21] and also in a double QPC [13]. In most experimental setups there is incoming wave both from the left and right. Here there is only an incoming wave from the left and therefore the AB oscillations are not seen in the single QPC system. The AB oscillations only happen inside the constriction of the first QPC because there the reflected wave from the second QPC interferes with the incoming wave. It is interesting to compare the paths taken by the electrons in Fig. 3.24 with the probability density seen in Fig. 3.20 as the circular path can be seen clearly.

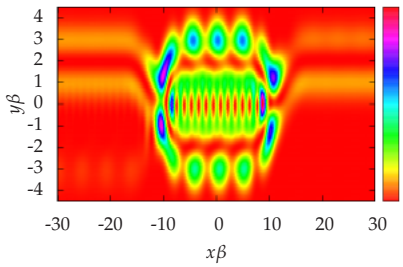

(a) Point **d** ($E/\hbar\Omega_\omega = 2.152$, $n = 1$, $B = 1.0\,\mathrm{T}$).

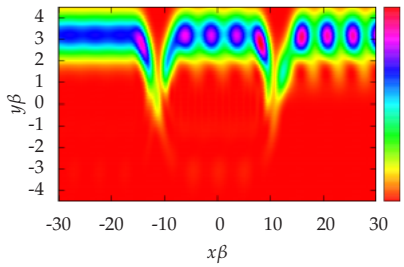

(b) Point **e** ($E/\hbar\Omega_\omega = 2.225$, $n = 0$, $B = 1.0\,\mathrm{T}$).

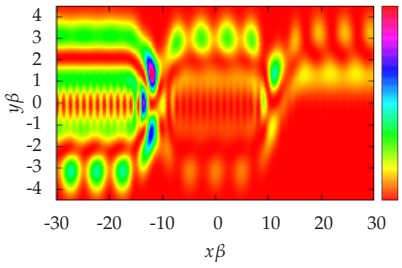

(c) Point **f** ($E/\hbar\Omega_\omega = 2.259$, $n = 0$, $B = 1.0\,\mathrm{T}$).

FIG. 3.20: Probability density for the peaks marked in Fig. 3.19d.

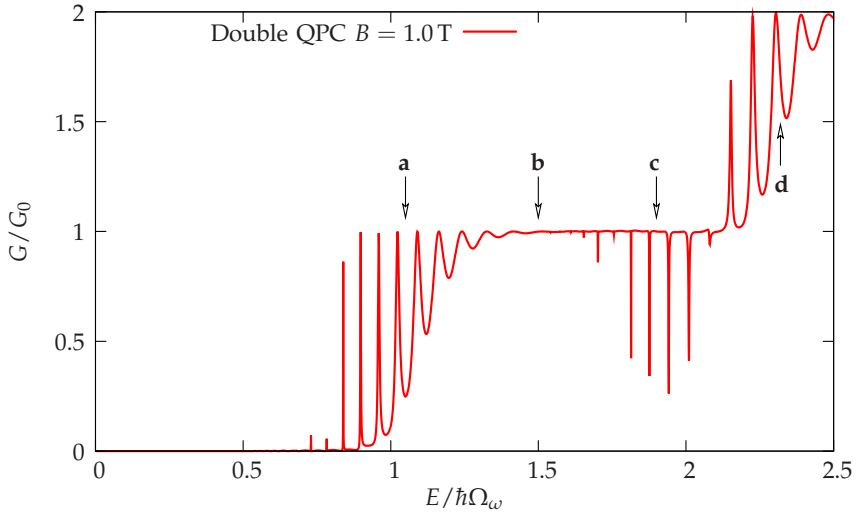

FIG. 3.21: The conductance of the double Quantum Point Contact in a magnetic field of 1.0 T. The points indicate energies where the conductance is plotted as a function of the magnetic field in Fig. 3.22.

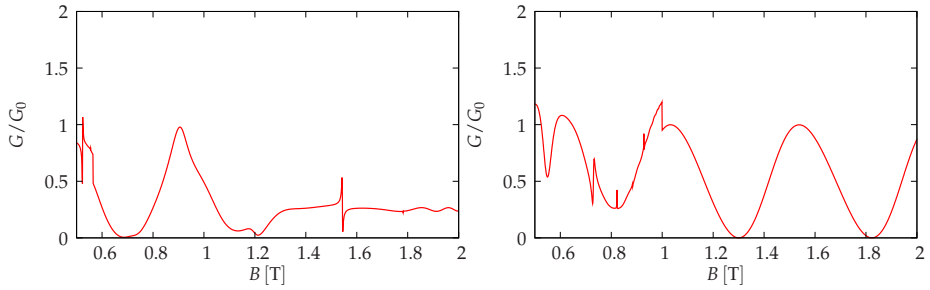

(a) Point **a** ($\frac{E}{\hbar\Omega_\omega(B=1.0\,\mathrm{T})} = 1.05$).

(b) Point **b** ($\frac{E}{\hbar\Omega_\omega(B=1.0\,\mathrm{T})} = 1.5$).

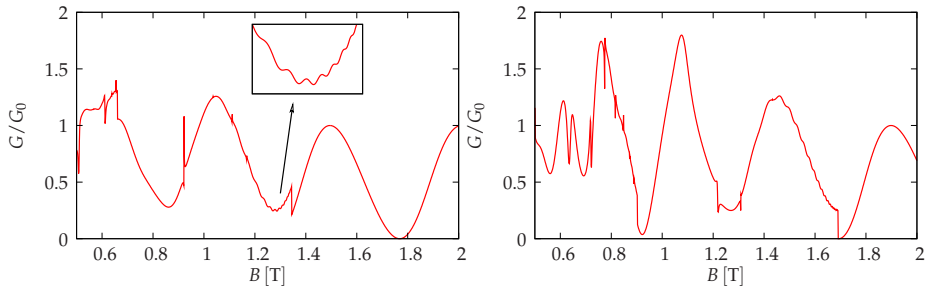

(c) Point **c** ($\frac{E}{\hbar\Omega_\omega(B=1.0\,\mathrm{T})} = 1.9$).

(d) Point **d** ($\frac{E}{\hbar\Omega_\omega(B=1.0\,\mathrm{T})} = 2.32$).

FIG. 3.22: The conductance through the double QPC as a function of the magnetic field. The absolute value of the energy is indicated in each sub-figure and marked in Fig. 3.21.

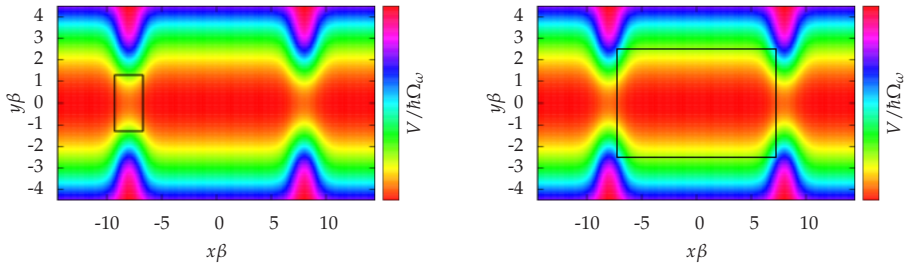

!ht

(a) Larger AB oscillations.

(b) Smaller AB oscillations.

FIG. 3.23: Area of the boxes for the AB oscillations in Fig. 3.22c.

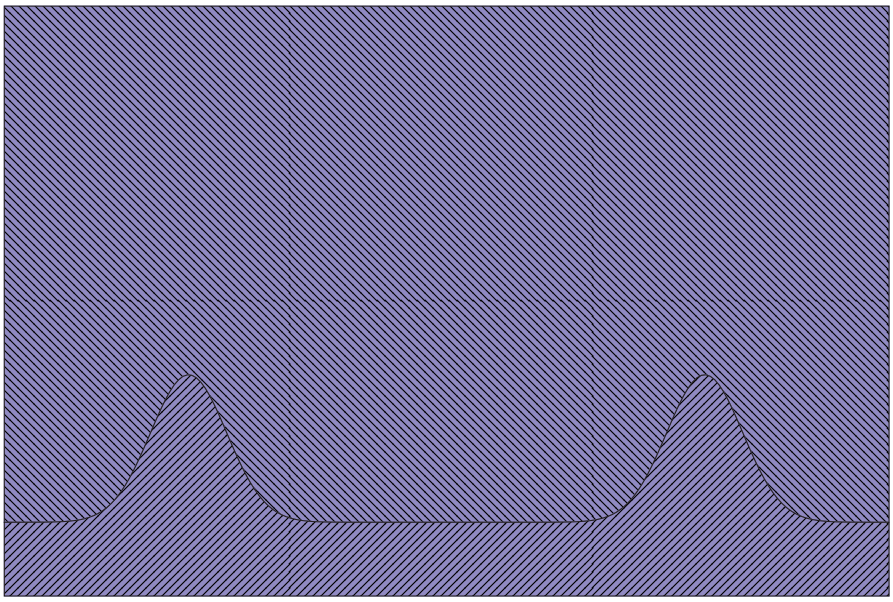

FIG. 3.24: The paths taking by electrons causing the AB oscillations in the double QPC.

3.3.2 Time-Harmonic Double Quantum Point Contact

A time-harmonic double QPC

$$\begin{aligned} V(x,y,t) = {} & V_{s1}e^{-\alpha_x(x-x_1)^2-\alpha_y(y-y_1)^2} && + V_{s2}e^{-\gamma_x(x-x_2)^2-\gamma_y(y-y_2)^2} \\ & + V_{s3}e^{-\eta_x(x-x_3)^2-\eta_y(y-y_3)^2} && + V_{s4}e^{-\nu_x(x-x_4)^2-\nu_y(y-y_4)^2} \\ & + V_{t1}e^{-\alpha_x(x-x_1)^2-\alpha_y(y-y_1)^2}\cos\omega t && + V_{t2}e^{-\gamma_x(x-x_2)^2-\gamma_y(y-y_2)^2}\cos\omega t \\ & + V_{t3}e^{-\eta_x(x-x_3)^2-\eta_y(y-y_3)^2}\cos\omega t && + V_{t4}e^{-\nu_x(x-x_4)^2-\nu_y(y-y_4)^2}\cos\omega t\,, \end{aligned} \tag{3.4}$$

with the parameters,

$$\begin{aligned} &V_{s1} = 6.0\,\text{meV}, \quad V_{t1} = 0.5\,\text{meV}, \quad \alpha_x = 0.5\beta_0^2, \quad \alpha_y = 0.3\beta_0^2, \quad x_1 = \;\; 8\beta_0, \quad y_1 = -3\beta_0, \\ &V_{s2} = 6.0\,\text{meV}, \quad V_{t2} = 0.5\,\text{meV}, \quad \gamma_x = 0.5\beta_0^2, \quad \gamma_y = 0.3\beta_0^2, \quad x_2 = \;\; 8\beta_0, \quad y_2 = \;\; 3\beta_0, \\ &V_{s3} = 6.5\,\text{meV}, \quad V_{t3} = 0.0\,\text{meV}, \quad \eta_x = 0.5\beta_0^2, \quad \eta_y = 0.3\beta_0^2, \quad x_3 = -8\beta_0, \quad y_3 = -3\beta_0, \\ &V_{s4} = 6.5\,\text{meV}, \quad V_{t4} = 0.0\,\text{meV}, \quad \nu_x = 0.5\beta_0^2, \quad \nu_y = 0.3\beta_0^2, \quad x_4 = -8\beta_0, \quad y_4 = \;\; 3\beta_0\,, \\ &\omega/\Omega_\omega = 0.17\,. \end{aligned}$$

This system is similar to the double QPC in seen in Fig. 3.15, except that now the first QPC is oscillating in time. The oscillation has been kept small ($\Delta V = 1.0\,\text{meV}$) to be able to see the deviations from the static case. The conductance through this system is presented in Fig. 3.25 with and without a magnetic field. The most noticeable change seen in the conductance is the shift in the peaks of the QBS. This is because the time-average height of the potential is lower than in the static case. Figure 3.26 shows an enlarged view of the conductance in a magnetic field of $B = 1.0\,\text{T}$. A number of smaller features can be seen there more clearly that are not seen in the static case. These resonances are due to inelastic scatterings induced by the potential. Some of these resonances are familiar, such as the ones located at $E/\hbar\Omega_\omega = 0.67$ and $E/\hbar\Omega_\omega = 0.85$ in Fig. 3.26a. These resonances are located ω and 2ω away from the subband edge respectively, and are due to the opening of a new conduction channel. Fano like resonances can also be seen in the conductance at $E/\hbar\Omega_\omega = 0.8985$, $E/\hbar\Omega_\omega = 0.950$, $E/\hbar\Omega_\omega = 1.006$ and $E/\hbar\Omega_\omega = 1.064$. In Fig. 3.27 the probability density at the point marked **a** in Fig. 3.26a is shown over one period at equally spaced intervals. The probability density is interesting as it show a QBS that rotates inside the cavity. The results presented here for this system are preliminary and further study will be continued in future.

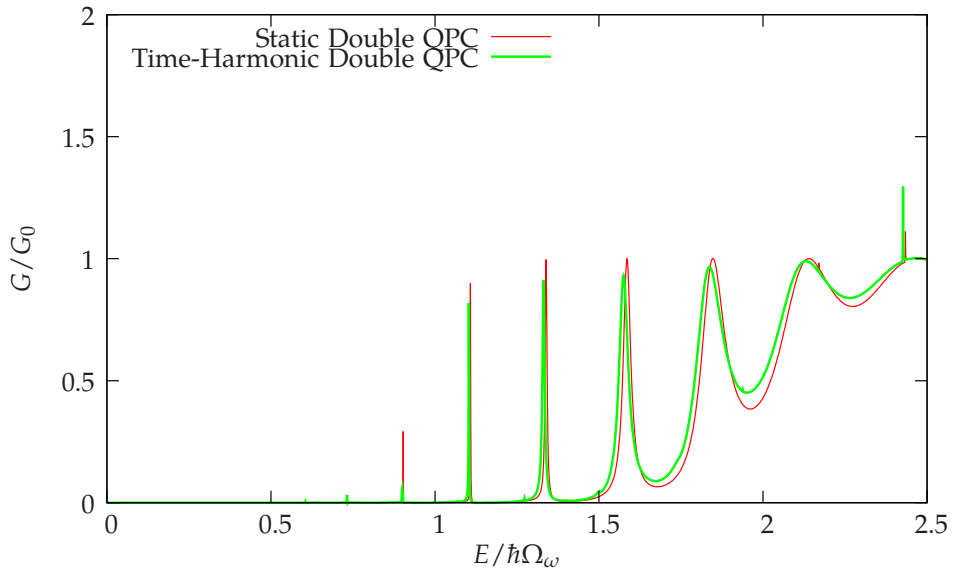

(a) $B = 0.0\,\mathrm{T}$

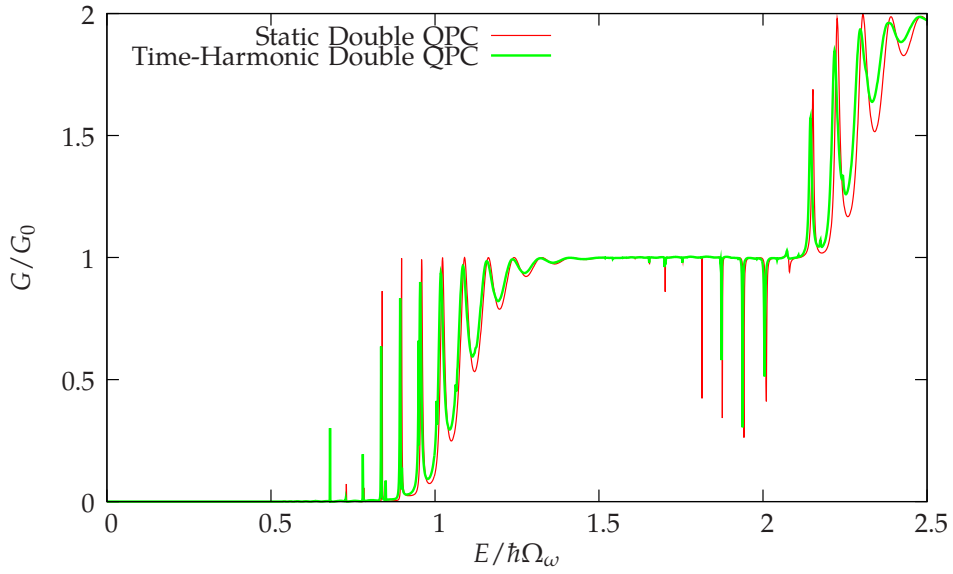

(b) $B = 1.0\,\mathrm{T}$

FIG. 3.25: The conductance of the time-harmonic double QPC.

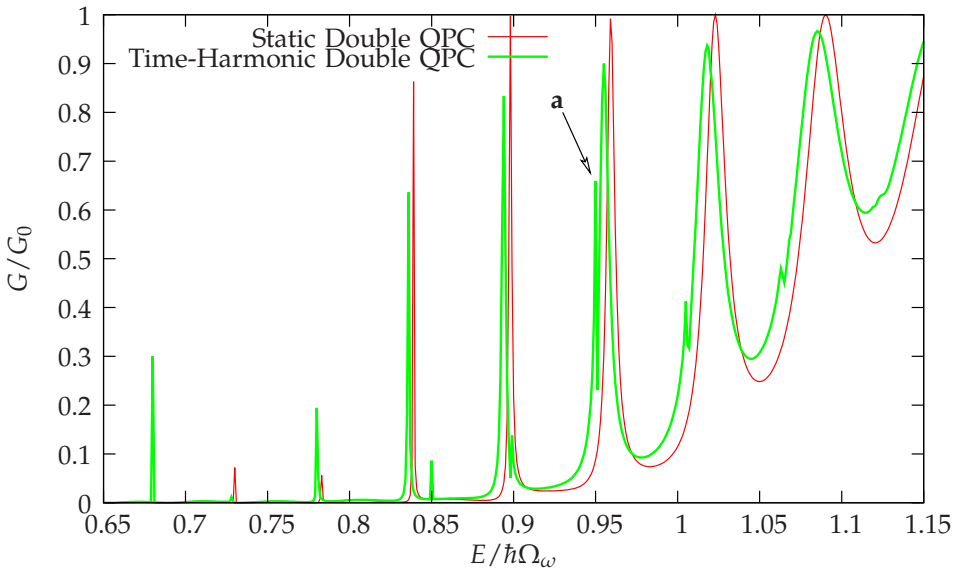

(a) First subband.

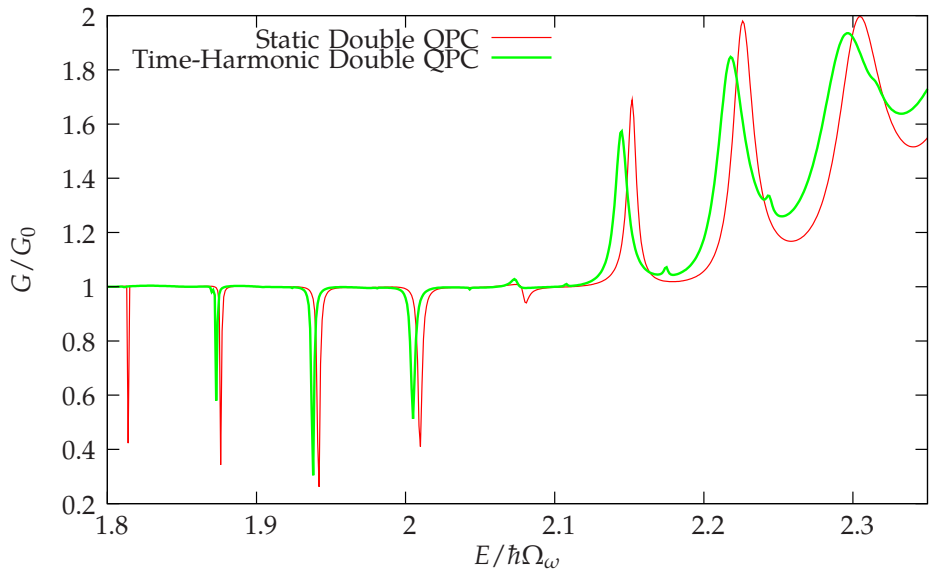

(b) Second subband.

FIG. 3.26: Enlarged view of the conductance of the time-harmonic double QPC in a magnetic field of $B = 1.0\,\mathrm{T}$.

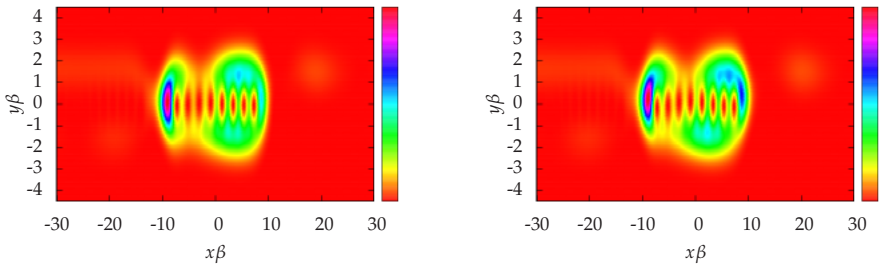

(a) $t\Omega_\omega = 0.00$ ($t = 0.00\,\mathrm{ps}$).

(b) $t\Omega_\omega = 2.96$ ($t = 0.97\,\mathrm{ps}$).

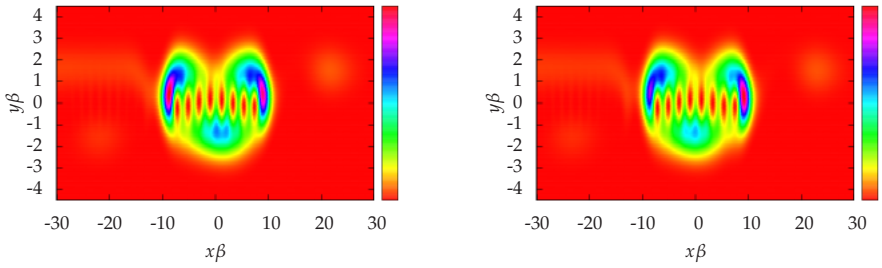

(c) $t\Omega_\omega = 6.28$ ($t = 2.07\,\mathrm{ps}$).

(d) $t\Omega_\omega = 9.24$ ($t = 3.05\,\mathrm{ps}$).

FIG. 3.27: Probability density for the double time-harmonic QPC at $E/\hbar\Omega_\omega = 0.950$, marked as point **a** in Fig. 3.26a.

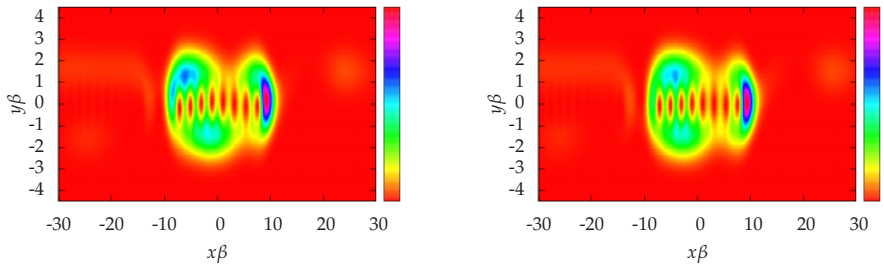

(e) $t\Omega_\omega = 12.20$ ($t = 4.02\,\mathrm{ps}$).

(f) $t\Omega_\omega = 15.52$ ($t = 5.12\,\mathrm{ps}$).

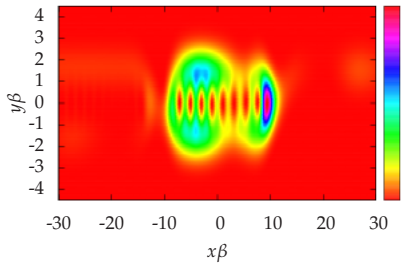

(g) $t\Omega_\omega = 18.48$ ($t = 6.10\,\mathrm{ps}$).

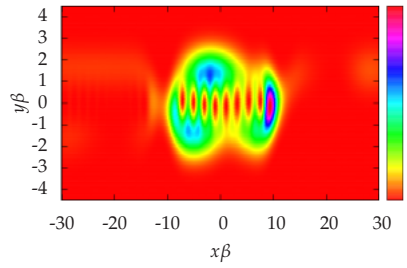

(h) $t\Omega_\omega = 21.44$ ($t = 7.07\,\mathrm{ps}$).

FIG. 3.27: Probability density for the double time-harmonic QPC at $E/\hbar\Omega_\omega = 0.950$, marked as point **a** in Fig. 3.26a.

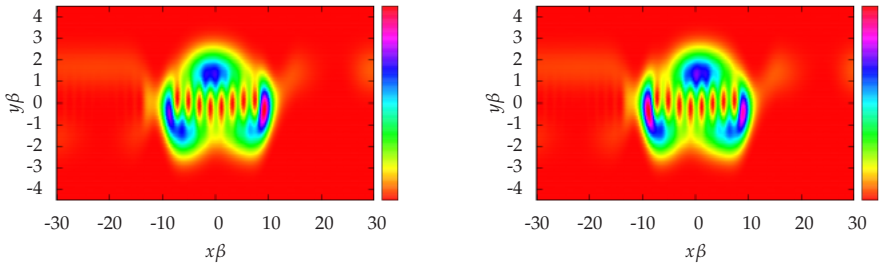

(i) $t\Omega_\omega = 24.76$ ($t = 8.16\,\text{ps}$).

(j) $t\Omega_\omega = 27.72$ ($t = 9.14\,\text{ps}$).

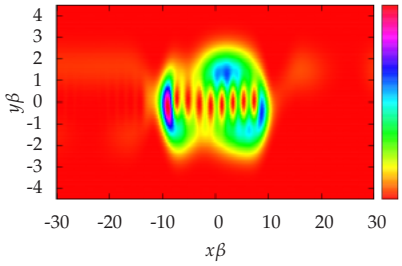

(k) $t\Omega_\omega = 30.68$ ($t = 10.11\,\text{ps}$).

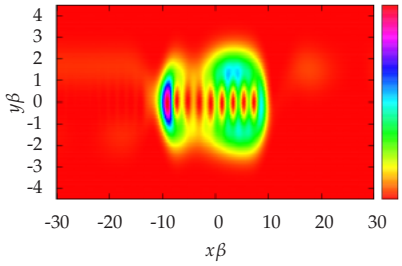

(l) $t\Omega_\omega = 34.00$ ($t = 11.21\,\text{ps}$).

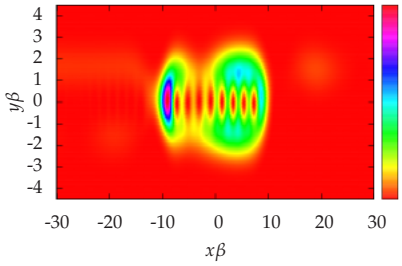

(m) $t\Omega_\omega = 36.96$ ($t = 12.19\,\text{ps}$).

FIG. 3.27: Probability density for the double time-harmonic QPC at $E/\hbar\Omega_\omega = 0.950$, marked as point **a** in Fig. 3.26a.

3.3.3 Double QPC with a Repulsive Gaussian in the Cavity

A static double QPC with a Gaussian hill in the middle of the cavity

$$\begin{aligned} V(x,y) &= V_1 e^{-\alpha_x(x-x_1)^2-\alpha_y(y-y_1)^2} + V_2 e^{-\gamma_x(x-x_2)^2-\gamma_y(y-y_2)^2} \\ &+ V_3 e^{-\eta_x(x-x_3)^2-\eta_y(y-y_3)^2} + V_4 e^{-\nu_x(x-x_4)^2-\nu_y(y-y_4)^2} \\ &+ V_5 e^{-\tau_x x^2-\tau_y y^2}, \end{aligned} \tag{3.5}$$

with the parameters,

$$\begin{aligned} &V_1 = 6.5\,\text{meV}, \quad \alpha_x = 0.5\beta_0^2, \quad \alpha_y = 0.3\beta_0^2, \quad x_1 = \ \ 8\beta_0, \quad y_1 = -3\beta_0, \\ &V_2 = 6.5\,\text{meV}, \quad \gamma_x = 0.5\beta_0^2, \quad \gamma_y = 0.3\beta_0^2, \quad x_2 = \ \ 8\beta_0, \quad y_2 = \ \ 3\beta_0, \\ &V_3 = 6.5\,\text{meV}, \quad \eta_x = 0.5\beta_0^2, \quad \eta_y = 0.3\beta_0^2, \quad x_3 = -8\beta_0, \quad y_3 = -3\beta_0, \\ &V_4 = 6.5\,\text{meV}, \quad \nu_x = 0.5\beta_0^2, \quad \nu_y = 0.3\beta_0^2, \quad x_4 = -8\beta_0, \quad y_4 = \ \ 3\beta_0, \\ &V_5 = 6.5\,\text{meV}, \quad \tau_x = 0.5\beta_0^2, \quad \tau_y = 0.5\beta_0^2, \end{aligned}$$

can be seen in Fig. 3.28 and the conductance is presented in Fig. 3.29. The conductance is

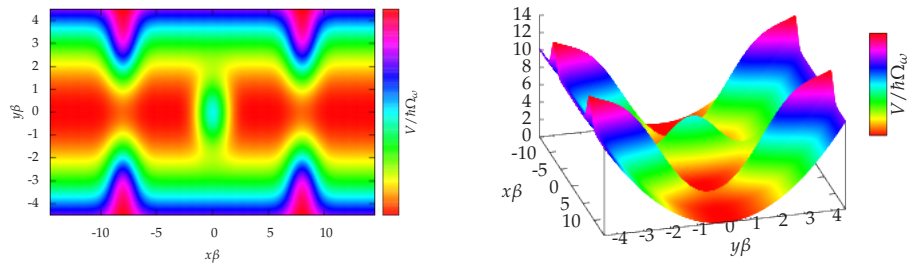

(a) Contour plot. (b) 3D plot.

FIG. 3.28: A plot of the double QPC with a repulsive Gaussian in the middle embedded in a wire with a parabolic confinement.

quite low when the strength of the magnetic field is low. Since then the incident wave collides almost directly with the center hill. When the strength of the magnetic field increases the Lorentz force starts to aid the conductance by making edge states similar to those seen in Fig. 3.14 that guide the electrons around the hill. The ring structure that forms can be seen in Fig. 3.31. The structure is not as simple as in the case of the Gaussian Ring [3] due to the size of the double QPC. In Fig. 3.30 the QBS marked in Fig. 3.29 can be seen. It seems to be more favourable for the QBS to form two small rings (Figs. 3.30a-3.30d) between the QPCs and the hill instead of a big ring around the Gaussian hill (Fig. 3.30e).

The probability density show interference between the hill and the QPCs along with mode mixing around the hill. In Fig. 3.30c the wave length is $\lambda\beta \approx 1.4$ and the distance between the minima in the interference between the QPC and the hill is on average $L\beta \approx 1.37$. This gives a ratio of $\lambda\beta/L\beta \approx 0.98$. The ellipse on the right has a major diameter of $a\beta \approx 9.14$ and a minor diameter of $b\beta \approx 4.94$. In Fig. 3.30e the distance between the two peaks is $L\beta \approx= 4.8$.

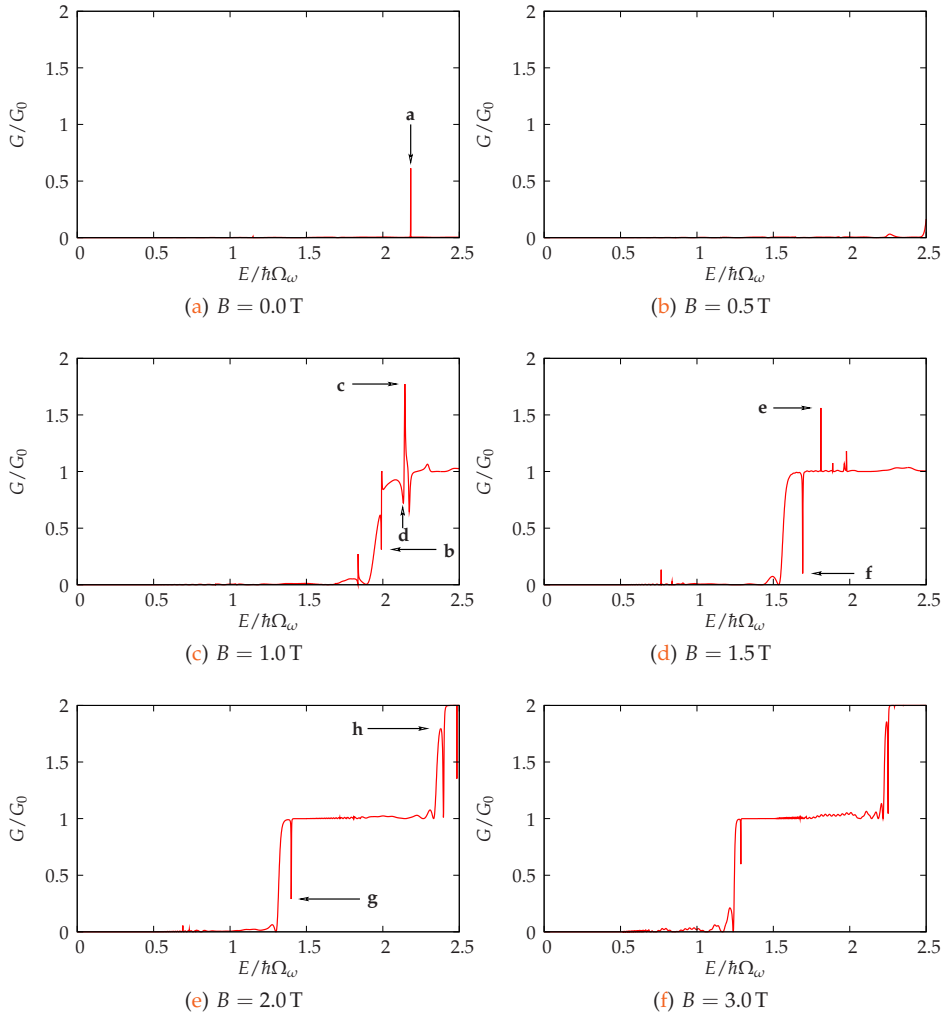

(a) $B = 0.0\,\mathrm{T}$ (b) $B = 0.5\,\mathrm{T}$

(c) $B = 1.0\,\mathrm{T}$ (d) $B = 1.5\,\mathrm{T}$

(e) $B = 2.0\,\mathrm{T}$ (f) $B = 3.0\,\mathrm{T}$

FIG. 3.29: The conductance of the double QPC with a Gaussian hill in the middle in a magnetic field.

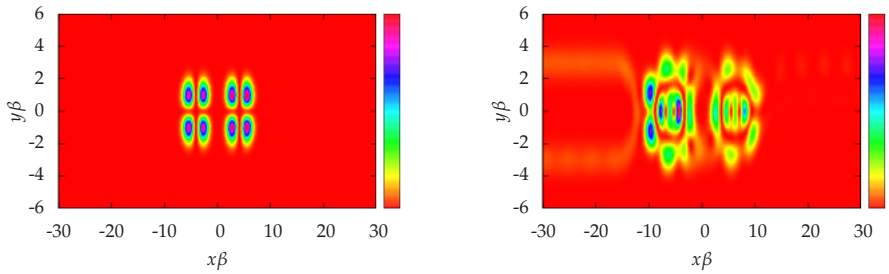

(a) Point **a** ($E/\hbar\Omega_\omega = 2.18212$, $n = 1$, $B = 0.0\,\mathrm{T}$). (b) Point **b** ($E/\hbar\Omega_\omega = 1.99053$, $n = 0$, $B = 1.0\,\mathrm{T}$).

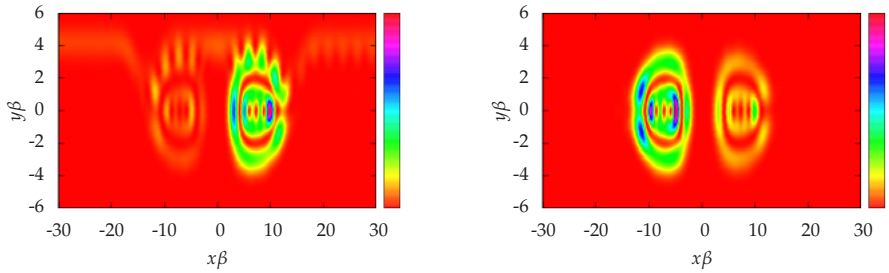

(c) Point **e** ($E/\hbar\Omega_\omega = 1.81084$, $n = 0$, $B = 1.5\,\mathrm{T}$). (d) Point **e** ($E/\hbar\Omega_\omega = 1.81084$, $n = 1$, $B = 1.5\,\mathrm{T}$).

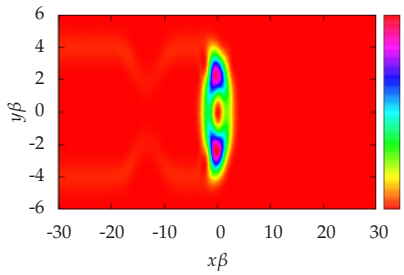

(e) Point **f** ($E/\hbar\Omega_\omega = 1.69184$, $n = 0$, $B = 1.5\,\mathrm{T}$).

FIG. 3.30: Quasi-bound states in the double QPC with a repulsive Gaussian in the Middle. The energies at which the probability density is calculated are indicated in each sub-figure and marked in Fig. 3.29.

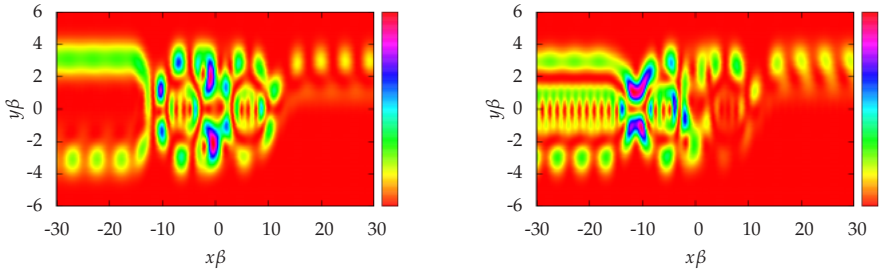

(a) Point **e** ($E/\hbar\Omega_\omega = 2.13455$, $n = 0$, $B = 1.0\,\mathrm{T}$). (b) Point **e** ($E/\hbar\Omega_\omega = 2.13455$, $n = 1$, $B = 1.0\,\mathrm{T}$).

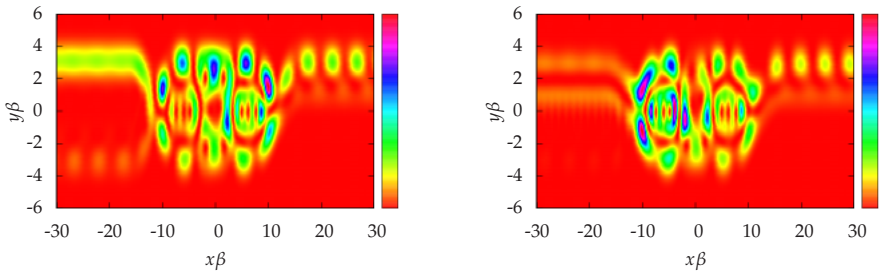

(c) Point **c** ($E/\hbar\Omega_\omega = 2.14404$, $n = 0$, $B = 1.0\,\mathrm{T}$). (d) Point **c** ($E/\hbar\Omega_\omega = 2.14404$, $n = 1$, $B = 1.0\,\mathrm{T}$).

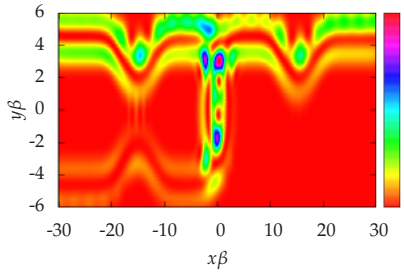

(e) Point **g** ($E/\hbar\Omega_\omega = 2.37847$, $n = 1$, $B = 2.0\,\mathrm{T}$).

FIG. 3.31: Probability density for the double QPC with a repulsive Gaussian hill. Points at which energies the probability density is calculated are marked in Fig. 3.29.

CHAPTER 4

Conclusion and Summary

In this thesis a time-dependent model for electron transport through a quantum wire was developed using the Lippmann-Schwinger scattering formalism and the Landauer-Büttiker formalism. The model describes sums of static and time-periodic Gaussian-shaped potentials are used to make complex geometries embedded in quantum wires. This model was then used to investigate the transport through five different types of structures, a time-harmonic Gaussian-shaped potential, a Gaussian-shaped well with a bottom oscillating periodically in time, a static single QPC, a double QPC and a static Gaussian-shaped hill placed inside a static double QPC. The model is capable of examining these structures both with and without a homogeneous perpendicular magnetic field with the use of a mixed momentum-coordinate representation [8].

The first structure investigated was a time-harmonic Gaussian-shaped potential. The conductance of this structure was very similar to the static case except dip-and-peak structures were observed when the incident electrons could make inelastic transitions to a subbands edge. In the case of a time-harmonic Gaussian-shaped well a Fano like resonance was observed. Which was due to the trapping of electrons in the well by an inelastic scattering processes.

The quantum point contact investigated showed that the conductance through it is quantised similar to the quantisation of the conductance through an ideal quantum wire. When a magnetic field was applied perpendicular to the QPC edge states were observed as the strength of the magnetic field increased, these states made the conductance of the QPC approach that of an idle wire. The double QPC showed more structure in the conductance than the single QPC due to quasi-bound states inside the cavity formed by the two QPCs and also exhibited the quantisation of the conductance like the single QPC. The addition

of the second QPC did not lower the conductance significantly. When a magnetic field was applied to the double QPC the electrons could execute a cyclotron motion inside the cavity and Aharonov-Bohm oscillations were observed even though the geometry of the system was singly connected. In the time-harmonic double QPC the QBS were shifted due to a weakening of one of the QPC on the average and resonances due to inelastic scatterings were observed. When a static Gaussian-shaped hill was placed inside the cavity of the double QPC the conductance was almost blocked at low magnetic fields where the electron wave collided almost directly with the center hill. When the strength of the magnetic field was increased AB type oscillations occur in the conductance. The probability density showed a rich structure with interference and mode mixing.

In general we have succeeded in constructing a model of the conduction of an electron wave through a smooth extended static and time-periodic embedded system in a quantum wire in an external magnetic field. The model will be used for studying quantum pumping and other interference phenomena in a realistic potential landscape mimicking experimental systems.

Appendices

A

Ideal Quantum Wire

A.1 States of a Quantum Wire in a Magnetic Field

It is important to know the states of a quantum wire that does not have an embedded scattering potential. These asymptotic states in the scattering sense can be used as a basis to describe the transport of a wire with an embedded scattering potential. Here these states will be found and some of their properties discussed.

The Hamiltonian for a ideal wire in a magnetic field is $H = H_0 + V_c(\vec{x})$, where

$$H_0 = \frac{1}{2m^*}\left[P + \frac{e}{c}\vec{A}(\vec{x})\right]^2 . \tag{A.1}$$

We choose $\vec{B}$ to be in the z-direction ($\vec{B} = Bz$) and use Landau gauge $\vec{A} = -By\vec{x}$. The Hamiltonian of the system is then

$$H_0 = \frac{1}{2m^*}\left[\frac{\hbar}{i}\nabla - eBy\vec{x}\right]^2 = -\frac{\hbar^2}{2m^*}\left[\nabla^2 - \frac{2i}{l^2}y\partial_x - \frac{y^2}{l^4}\right] . \tag{A.2}$$

The constant l is called the magnetic length and is given by

$$l^2 = \frac{\hbar}{eB} . \tag{A.3}$$

We choose the confinement potential to be parabolic,

$$V_c(y) = \frac{1}{2}m^*\Omega_0^2 y^2 , \tag{A.4}$$

giving use the total Hamiltonian

$$H = H_0 + V_c(y) = -\frac{\hbar^2}{2m^*}\left[\nabla^2 - \frac{2i}{l^2}y\partial_x - \frac{y^2}{l^4}\right] + \frac{1}{2}m^*\Omega_0^2 y^2 . \tag{A.5}$$

As there is no time dependence it is enough to solve the time-independent Schrödinger equation

$$H\Psi(x,y) = E\Psi(x,y)\,. \tag{A.6}$$

To be able to separate the Schrödinger equation we must go to a mixed momentum-coordinate representation [8] by doing a Fourier transformation on the x-coordinate

$$\Psi(x,y) = \int \frac{\mathrm{d}p}{2\pi}\, e^{ipx}\Psi(p,y)\,, \tag{A.7}$$

This Fourier transformation of the x-coordinate yields

$$\int \frac{\mathrm{d}p}{2\pi}\left\{-\frac{\hbar^2}{2m^*}\left[p^2\partial_y^2 + \frac{2p}{l^2}y - \frac{y^2}{l^4}\right] + \frac{1}{2}m^*\Omega_0^2 y^2\right\}\Psi(p,y) = E\int \frac{\mathrm{d}p}{2\pi} e^{ipx}\Psi(p,y)\,. \tag{A.8}$$

We can simplify the above equation by completing in the square

$$\frac{\hbar^2 y^2}{2m^* l^4} + \frac{1}{2}m^*\Omega_0^2 y^2 - \frac{\hbar^2 p}{m^* l^2}y + \frac{\hbar^2 p^2}{ml^2}y + \frac{\hbar^2 p^2}{2m^*} = \frac{1}{2}m^*\Omega_\omega^2(y-y_0)^2 + \frac{\hbar^2}{2m^*}p^2\left(1 - \frac{\omega_c^2}{\Omega_\omega^2}\right), \tag{A.9}$$

where $\omega_c = \frac{eB}{m^*}$, $\Omega_\omega^2 = \omega_c^2 + \Omega_0^2$ and $y_0 = \frac{\hbar p\omega_c}{m^*\Omega_\omega^2}$.
Then by transforming the whole equation with $\int \mathrm{d}x\, e^{iqx}$ we obtain

$$\left\{-\frac{\hbar^2}{2m^*}\partial_y^2 + \frac{1}{2}m^*\Omega_\omega^2(y-y_0)^2\right\}\Psi(q,y) = \left(E - \frac{\hbar^2}{2m^*}q^2\frac{\Omega_0^2}{\Omega_\omega^2}\right)\Psi(q,y)\,. \tag{A.10}$$

This is just the harmonic oscillator with frequency Ω_ω and center coordinate y_0. The solution is trivial and can be found in any elementary text book on quantum mechanics [22],

$$\psi_n(q,y) = \left(\frac{\beta^2}{\pi}\right)^{\frac{1}{4}}\frac{1}{\sqrt{2^n n!}}e^{-\beta^2\frac{(y-y_0)^2}{2}}H_n(\beta(y-y_0))\,. \tag{A.11}$$

Where $H_n(y)$ is the Hermite polynomial of order n [23] and the constant β has the dimension of inverse length and is given by

$$\beta^2 = \frac{m\Omega_\omega}{\hbar}\,. \tag{A.12}$$

This constant is the reciprocal of the effective magnetic length in the system and it includes the magnetic length l in Eq. A.3. This can be seen by rewriting β as

$$\beta^2 = \frac{m^*}{\hbar}\sqrt{\omega_c^2 + \Omega_0^2} = \sqrt{\frac{e^2B^2}{\hbar^2} + \frac{(m^*)^2}{\hbar^2}\Omega_0^2} = \sqrt{\frac{1}{l^4} + \frac{(m^*)^2}{\hbar^2}\Omega_0^2}\,. \tag{A.13}$$

The energy of the system is

$$E_n(q) = E_n + \frac{\hbar^2}{2m}q^2\frac{\Omega_0^2}{\Omega_\omega^2}\,, \tag{A.14}$$

where $E_n = (n+1/2)\hbar\Omega_\omega$.

A.2 Bound States in a Finite Wire

We now want to examine a finite wire with a parabolic confinement that does not have an embedded scattering potential. The bound states of this wire can be compared with the quasi-bound states of structures embedded in a wire. The Schrödinger equation for a finite wire with a parabolic confinement is

$$\left\{-\frac{\hbar^2}{2m^*}\nabla^2+\frac{1}{2}m^*\Omega_0^2y^2+W(x)\right\}\psi(x,y)=E\psi(x,y)\,. \tag{A.15}$$

Where $W(x)$ is the infinite square well potential in the x-direction

$$W(x)=\begin{cases}0, & -L/2\leq x\leq L/2,\\ \infty, & x<-L/2, x>L/2,\end{cases} \tag{A.16}$$

and L is the length of the wire. Equation (A.15) is not coupled in the coordinates and we can use separation of variables to solve the equation, $\psi(x,y)=\varphi(x)\phi(y)$. It is easy to see that $\phi(y)$ is just the eigenfunction for the harmonic oscillator and that $\varphi(x)$ is the eigenfunction for the infinite square well. The allowed energies of the system are then given by the sum of the energies of the two

$$E_{nj}=\hbar\Omega_\omega(n+\frac{1}{2})+\frac{j^2\pi^2\hbar^2}{2m^*L^2}\,, \tag{A.17}$$

scaling the variables yields

$$\frac{E_{nj}}{\hbar\Omega_\omega}=\left(\frac{1}{2}+n\right)+\frac{j^2\pi^2}{2(L\beta)^2}\,,$$

or

$$\widehat{E}_{nj}=\left(\frac{1}{2}+n\right)+\frac{j^2\pi^2}{2\widehat{L}^2}\,. \tag{A.18}$$

B

Matrix Elements for the Potential

In this appendix the analytical calculations for the matrix elements of the potential will be shown. The shape of the potential has been chosen to be Gaussian and is given by

$$V(x,y) = Ve^{-\alpha_x(x-x_c)^2-\alpha_y(y-y_c)^2}\,, \tag{B.1}$$

where V is the strength, $(x_c,\, y_c)$ are the center coordinates and $(\alpha_x,\, \alpha_y)$ control the range of the potential. The matrix elements of the potential are given by

$$V_{nn'}(q,p) = \int \mathrm{d}y\, \phi_n^*(y,q) V(q-p,y) \phi_{n'}(y,p)\,, \tag{B.2}$$

where

$$\begin{aligned} V(q-p,y) &= \int \mathrm{d}x\, e^{-i(q-p)x} V e^{-\alpha_x(x-x_c)^2-\alpha_y(y-y_c)^2} \\ &= V e^{-\alpha_y(y-y_c)^2} \int_{-\infty}^{\infty} \mathrm{d}x\, e^{-\alpha_x(x-x_c)^2-i(q-p)x}\,. \end{aligned} \tag{B.3}$$

We start by calculating $V(q-p,y)$ by completing the square in the exponential

$$\alpha_x(x-x_c)^2 + i(q-p)x = a(x+b)^2 - x_{fac} = \alpha_x\left(x + \frac{i(q-p)-2\alpha_x x_c}{2\alpha_x}\right)^2 - x_{fac}\,, \tag{B.4}$$

where

$$x_{fac} = -\alpha_x x_c^2 + \frac{(i(q-p)-2\alpha_x x_c)^2}{4\alpha_x}\,.$$

Using the above we obtain

$$V(q-p,y) = V e^{-\alpha_y(y-y_c)^2} e^{x_{fac}} \int_{-\infty}^{\infty} \mathrm{d}x\, e^{-\alpha_x(x+\frac{i(q-p)-2\alpha_x x_c}{2\alpha_x})^2}\,, \tag{B.5}$$

i.e. a trivial Gaussian integral with the solution

$$V(q-p,y) = V\sqrt{\frac{\pi}{\alpha_x}} e^{-\alpha_y(y-y_c)^2} e^{x_{fac}}\,. \tag{B.6}$$

We now insert $V(q-p,y)$ into Eq. (B.2) and use Eq. (A.11) to get

$$V_{nn'}(q,p) = \frac{1}{\sqrt{\pi}}\frac{1}{\sqrt{2^{n+n'}n!n'!}}V\sqrt{\frac{\pi}{\alpha_x}}e^{x_{fac}} \times \int \beta \mathrm{d}y\, e^{-\beta^2\frac{1}{2}((y-y_0(q))^2+(y-y_0(p))^2)-\alpha_y(y-y_c)^2}H_n(\beta(y-y_0(q)))H_{n'}(\beta(y-y_0(p)))\,. \tag{B.7}$$

Rearranging terms and scaling we arrive at

$$\widehat{V}_{nn'}(q,p) = \widehat{V}\frac{\beta}{\sqrt{\alpha_x}}\frac{1}{\sqrt{2^{n+n'}n!n'!}}e^{x_{fac}}\times \times \int \beta \mathrm{d}y\, e^{-\beta^2\frac{1}{2}((y-y_0(q))^2+(y-y_0(p))^2)-\alpha_y(y-y_c)^2}H_n(\beta(y-y_0(q)))H_{n'}(\beta(y-y_0(p)))\,, \tag{B.8}$$

where $\widehat{V}_{nn'}(q,p) = 2\frac{(\hbar\Omega_\omega)^2}{(\hbar\Omega_0)^2}\frac{\beta}{\hbar\Omega_\omega}V_{nn'}$ and $\widehat{V} = 2\frac{(\hbar\Omega_\omega)^2}{(\hbar\Omega_0)^2}\frac{V}{\hbar\Omega_\omega}$.
We shall now take a closer look at the y integral and start by writing

$$-\frac{1}{2}(S-S_q)^2-\frac{1}{2}(S-S_p)-\frac{\alpha_y}{\beta^2}(S-S_c)^2 = -a(S-b)^2+c = -aS^2+2abS-ab^2+c \tag{B.9}$$

where $S=\beta y$, $S_q=\beta y_0(q)$, $S_p=\beta y_0(p)=\frac{q}{\beta}\frac{\omega_c}{\Omega_\omega}$, $S_c=\beta y_c$,
$a=(1+\frac{\alpha_y}{\beta^2})$, $b=\frac{S_q+S_p+2\frac{\alpha_y}{\beta^2}S_c}{2a}$ and $c=\frac{(S_q+S_p+2\frac{\alpha_y}{\beta^2}S_c)^2}{4a}-\frac{1}{2}(S_q^2+S_p^2-2\frac{\alpha_y}{\beta^2}S_c^2)$.
This gives us

$$\mathrm{I} = e^{\frac{(S_q+S_p+2\frac{\alpha_y}{\beta^2}S_c)^2}{4a}-\frac{1}{2}(S_q^2+S_p^2-2\frac{\alpha_y}{\beta^2}S_c^2)}\int \beta \mathrm{d}y\, e^{-(u-\frac{S_q+S_p}{2\sqrt{a}})^2}H_n(\frac{u}{\sqrt{a}}-S_q)H_{n'}(\frac{u}{\sqrt{a}}-S_p)\,, \tag{B.10}$$

where $u=\sqrt{a}S$. By use of (GR. 8.958.2) [24] we can write the Hermite Polynomials as a function of a single argument, i.e.

$$\mathrm{I} = \frac{1}{\sqrt{a}}e^{z^2-\frac{1}{2}(S_q^2+S_p^2-2\frac{\alpha_y}{\beta^2}S_c^2)}\frac{1}{\sqrt{2^{n+n'}}}\sum_{k=0}^{n}\sum_{k'=0}^{n'}\binom{n}{k}\binom{n'}{k'}H_k(-\sqrt{2}S_q)H_{k'}(-\sqrt{2}S_p)\times \times \int \mathrm{d}u\, e^{-(u-z)^2}H_{n-k}(\sqrt{\frac{2}{a}}u)H_{n'-k'}(\sqrt{\frac{2}{a}}u)\,, \tag{B.11}$$

where $z=\frac{S_q+S_p+2\frac{\alpha_y}{\beta^2}S_c}{2\sqrt{a}}$.
The integral over the exponential and the Hermite polynomials can now be done using (GR. 7.374.9) [24]

$$\mathrm{I} = \sqrt{\frac{\pi}{a}}e^{z^2-\frac{1}{2}(S_q^2+S_p^2-2\frac{\alpha_y}{\beta^2}S_c^2)}\sum_{k=0}^{n}\sum_{k'=0}^{n'}\sum_{l=0}^{min(n-k,n'-k')}\times \times \binom{n}{k}\binom{n'}{k'}\binom{n-k}{l}\binom{n'-k'}{l}2^l l!\times \times H_k(-\sqrt{2}S_q)H_{k'}(-\sqrt{2}S_p)(1-\frac{2}{a})^{\frac{n-k+n'-k'}{2}-l}H_{n-k+n'-k'-2l}\left[\frac{\sqrt{2/a}z}{\sqrt{1-2/a}}\right]\,. \tag{B.12}$$

The analytical expression for the matrix element is then

$$\widehat{V}_{nn'}(q,p) = \widehat{V}\sqrt{\frac{\beta^2\pi}{a\alpha_x}}\frac{1}{2^{n+n'}\sqrt{n!n'!}}e^{z^2-\frac{1}{2}(S_q^2+S_p^2-2\alpha_y/\beta^2 S_c^2)}e^{-\alpha_x/\beta^2\beta^2 x_c^2+\frac{(i(q/\beta^2-p/\beta^2)-2\alpha_x/\beta^2\beta^2 x_c)^2}{4\alpha_x/\beta^2}}\times$$
$$\times\sum_{k=0}^{n}\sum_{k'=0}^{n'}\sum_{l=0}^{min(n-k,n'-k')}\binom{n}{k}\binom{n'}{k'}\binom{n-k}{l}\binom{n'-k'}{l}2^l l!\times$$
$$\times H_k(-\sqrt{2}S_q)H_{k'}(-\sqrt{2}S_p)(1-\frac{2}{a})^{\frac{n-k+n'-k'}{2}-l}H_{n-k+n'-k'-2l}\left[\frac{z\sqrt{2/a}}{\sqrt{1-2/a}}\right]. \tag{B.13}$$

C

Floquet Theory

Floquet theory is a branch of theory of ordinary differential equations and states that a system with a time periodic potential will have a complete set of states [25, 26]

$$|\Phi_n(x,y,t)\rangle = e^{-(i\varepsilon_n/\hbar)t}|u_n(x,y,t)\rangle\,, \tag{C.1}$$

where $|u_n(t+T)\rangle = |u_n(t)\rangle$ and T is the period of the system. The state $|u_n(t)\rangle$ is called the Floquet state and the quantities ε_n is referred to as the quasi-energy.
It is interesting to compare this equation to the ones derived in chapter 2. If we expand the time-part of the periodic Floquet state in a Fourier series with frequency ω and construct the full wave function by summing over all states, we have

$$|\Psi(x,y,t)\rangle = \sum_{m\,n} e^{-i(\varepsilon_n/\hbar+m\omega)t}|\varphi_n^m(x,y)\rangle\,. \tag{C.2}$$

Comparing this equation with Eq. (2.34) we see that

$$|\varphi_n^m\rangle = \int \frac{dq}{2\pi}\phi_{n'}(q,y)e^{iqx}G_{n'}^{m'}(q)T_{n'n}^{m'0}(q,k_n^0) \tag{C.3}$$

and that the quasi-energy (ε_n) is equal to the incident energy (E_0) of the electrons.

C.1 Green's Function

In operator form the time-dependant Schrödinger equation is

$$i\hbar\partial_t|\Psi(t)\rangle = H(t)|\Psi(t)\rangle \tag{C.4}$$

where $H(t) = H_0 + V(t)$. Using Eq. (C.2) and expanding the time part of the potential in a Fourier series we have

$$\sum_m e^{-i(E_0/\hbar+m\omega)t}(E_0+\hbar m\omega - H_0)|\varphi^m\rangle = \sum_{sm} e^{-i(E_0/\hbar+(m+s)\omega)t}V^s|\varphi^m\rangle \tag{C.5}$$

To get rid of the time-dependence we multiply the above equation with $e^{i(E_0/\hbar)t}(e^{-im'\omega}t)^*$ and integrate over t from 0 to T. We can then write Eq. (C.4) as

$$(E_0 + \hbar m\omega - H_0)|\varphi^m\rangle = \sum_{m'} V^{m-m'}|\varphi^{m'}\rangle \tag{C.6}$$

We now define the Green's function as

$$G^m(E_0) = \frac{1}{E_0 + \hbar m\omega - H_0}\,, \tag{C.7}$$

The solution to Eq. (C.6) is then

$$|\varphi^m\rangle = |\varphi^0\rangle + G^m(E_0)\sum_{m'} V^{m-m'}|\varphi^{m'}\rangle\,. \tag{C.8}$$

We can see that this is a solution by applying $(G_n^m)^{-1}(E_0 + \hbar m\omega)$ to the solution as we then obtain Eq. (C.6) again. Equation (C.8) is same as Eq. (2.29), i.e. the Lippmann-Schwinger equation for the Fourier components of the wave function.

C.2 T-matrix

Suppressing the summation in Eq. (C.8), we have

$$\varphi = \varphi^0 + GV\varphi\,, \tag{C.9}$$

we assume an operator T, of the resolvent type such that

$$\varphi = (1 + GT)\varphi_0\,, \tag{C.10}$$

where we have defined the operator T as

$$T = V + VGT\,. \tag{C.11}$$

We now write this equation in mixed momentum-coordinate representation by using

$$\langle qn'm'|T|pnm\rangle = \langle qn'm'|V|pnm\rangle + \langle qn'm'|VGT|pnm\rangle\,, \tag{C.12}$$

where

$$\langle x|p\rangle = e^{ipx} \quad , \quad \langle y|nm\rangle = \phi(y, k_n^m)\,, \tag{C.13}$$

and use of the unity operator twice

$$1 = \sum_{n\,m}\int \frac{\mathrm{d}k}{2\pi}|knm\rangle\langle knm|$$

yields

$$\langle qn'm'|T|pnm\rangle = \langle qn'm'|V|pnm\rangle + \sum_{rs\,r's'}\int \frac{\mathrm{d}k}{2\pi}\frac{\mathrm{d}k'}{2\pi}\,\langle qn'm'|V|krs\rangle\langle krs|G|k'r's'\rangle\langle k'r's'|T|pnm\rangle\,.$$

(C.14)

The Green's function includes H_0 which is composed of the kinetic part and the confinement potential (in a magnetic field), therefore we have

$$H_0|knm\rangle = \left((n+\frac{1}{2})\hbar\Omega_\omega + \frac{\hbar^2}{2m}\frac{\Omega_0^2}{\Omega_\omega^2}k^2\right)|knm\rangle \tag{C.15}$$

which gives for the Green's function

$$\langle k'n'm'|G^m(E_0)|knm\rangle = \langle k'n'm'|knm\rangle \frac{1}{E_0 + \hbar m\omega - (n+\frac{1}{2})\hbar\Omega_\omega - \frac{1}{2}\left(\frac{k}{\beta}\right)^2 \frac{(\hbar\Omega_0)^2}{\hbar\Omega_\omega}} \,. \tag{C.16}$$

$$\begin{aligned}\langle k'n'm'|G^m(E_0)|knm\rangle &= 2\pi\delta(k'-k)\delta_{n'n}\delta_{m'm}2\frac{\hbar\Omega_\omega}{(\hbar\Omega_0)^2}\frac{1}{(k_n^m/\beta)^2-(k/\beta)^2} \\ &= 2\frac{(\hbar\Omega_\omega)^2}{(\hbar\Omega_0)^2)}\frac{2\pi}{\hbar\Omega_\omega}\delta(k'-k)\delta_{n'n}\delta_{m'm}G_n^m(k)\end{aligned} \tag{C.17}$$

Plugging the above into Eq. (C.14) we arrive at

$$T_{n'n}^{m'm}(q,p) = V_{n'n}^{m'-m}(q,p) + \sum_{rs}\int\frac{\mathrm{d}k}{2\pi}V_{n'r}^{m'-s}(q,k)G_r^s(k)T_{rn}^{sm}(k,p)\,, \tag{C.18}$$

i.e. the equation for the T-matrix as in Eq. (2.32).

D

Numerical Work

In this appendix it will be shown how the T-matrix equation (Eq. 2.32) is prepared for numerical calculations. The equation is turned into a set of linear algebraic equations that are easily solved with the help of a computer. This transformation is done by using a four point Gaussian integration on the integral that appears in the equation. But before this transformation can be done the poles of the Green's function must be taken care of. Most of the work done in this appendix is based on earlier work done by Jens H. Bárðarson [27].

D.1 Poles in the Green's Function

The Green's functions has an undetermined number of poles and appears in the integral equation for the T-matrix (Eq. 2.41). These poles must be taken into account during the integration to obtain the correct results. This section shows how they are dealt with.
The Green's function is

$$G_n^m(k) = \frac{1}{(k_n^m)^2 - k^2 + i\eta} \quad , \quad \eta \to 0^+ \tag{D.1}$$

where k_n^m and k are dimensionless, namely $k \to k/\beta$. We now use the fact that [28]

$$\frac{1}{x + i\eta} = \frac{\mathcal{P}}{x} - i\pi\delta(x)\,, \tag{D.2}$$

where $\mathcal{P}$ donates the Cauchy principle-value [29]. Using this we obtain

$$\int_{-\infty}^{\infty} \frac{f(k)\,\mathrm{d}k}{(k_n^m)^2 - k^2 + i\eta} = \mathcal{P}\int_{-\infty}^{\infty} \frac{f(k)\,\mathrm{d}k}{(k_n^m)^2 - k^2} - \int_{-\infty}^{\infty} i\pi f(k)\delta((k_n^m)^2 - k^2)\,\mathrm{d}k\,, \tag{D.3}$$

where $f(k)$ is some function that is multiplied with the Green function in the integral. Observing that we can write

$$\delta((k_n^m)^2 - k^2) = \frac{1}{2|k_n^m|}(\delta(k + k_n^m) + \delta(k - k_n^m))\,, \tag{D.4}$$

which yields

$$\int_{-\infty}^{\infty} \frac{f(k)\,\mathrm{d}k}{(k_n^m)^2 - k^2} = \mathcal{P}\int_{-\infty}^{\infty} \frac{f(k)\,\mathrm{d}k}{(k_n^m)^2 - k^2} - \frac{i\pi}{2|k_n^m|}\left(f(k_n^m) + f(-k_n^m)\right). \tag{D.5}$$

We know that

$$\int_{-\infty}^{\infty} \frac{\mathrm{d}k}{(k_n^m)^2 - k^2} = 0 \quad \Rightarrow \quad \int_{-\infty}^{\infty} \frac{f(\pm k_n^m)\,\mathrm{d}k}{(k_n^m)^2 - k^2} = 0\,, \tag{D.6}$$

and we can add this zero to the principle integral without effecting it

$$\mathcal{P}\int_{-\infty}^{\infty} \frac{f(k)\,\mathrm{d}k}{(k_n^m)^2 - k^2} = \int_0^{\infty} \frac{f(k) - f(k_n^m)}{(k_n^m)^2 - k^2}\,\mathrm{d}k + \int_0^{\infty} \frac{f(-k) - f(-k_n^m)}{(k_n^m)^2 - k^2}\,\mathrm{d}k\,. \tag{D.7}$$

We then have the final equation

$$\begin{aligned}\int_{-\infty}^{\infty} \frac{f(k)\,\mathrm{d}k}{(k_n^m)^2 - k^2} &= \int_0^{\infty} \frac{f(k) - f(k_n^m)}{(k_n^m)^2 - k^2}\,\mathrm{d}k + \int_0^{\infty} \frac{f(-k) - f(-k_n^m)}{(k_n^m)^2 - k^2}\,\mathrm{d}k \\ &- \frac{i\pi}{2|k_n^m|}\left(f(k_n^m) + f(-k_n^m)\right).\end{aligned} \tag{D.8}$$

It should be noted that this is not needed for the non-propagating modes since the Green's function is not singular for those modes, as the wavevector is imaginary in those cases.

D.2 Algebraic Equations

We will now use Eq. (D.8) to turn Eq. (2.32) into a set of algebraic equations. Recall from Eq. (2.41)

$$\begin{aligned}\widehat{T}_{n'n}^{m'm}(q,p) &= \widehat{V}_{s,n'n}(q,p)\delta_{m'-m,0} + \frac{1}{2}\widehat{V}_{t,n'n}(q,p)(\delta_{m'-m,-1} + \delta_{m'-m,1}) \\ &+ \sum_r \int \frac{\mathrm{d}k}{2\pi}\,\widehat{V}_{s,n'r}(q,k)G_r^{m'}(k)\widehat{T}_{rn}^{m'}(k,p) \\ &+ \sum_r \int \frac{\mathrm{d}k}{2\pi}\,\frac{1}{2}\widehat{V}_{t,n'r}(q,k)G_r^{m'+1}(k)\widehat{T}_{rn}^{m'+1}(k,p) \\ &+ \sum_r \int \frac{\mathrm{d}k}{2\pi}\,\frac{1}{2}\widehat{V}_{t,n'r}(q,k)G_r^{m'-1}(k)\widehat{T}_{rn}^{m'-1}(k,p) \\ &= \widehat{T}_b + \widehat{T}_s + \widehat{T}_t\,,\end{aligned} \tag{D.9}$$

where

$$\widehat{T}_b = \widehat{V}_{s,n'n}(q,p)\delta_{m'-m,0} + \frac{1}{2}\widehat{V}_{t,n'n}(q,p)(\delta_{m'-m,-1} + \delta_{m'-m,1})\,, \tag{D.10}$$

$$\widehat{T}_s = \sum_r \int \frac{\mathrm{d}k}{2\pi}\,\widehat{V}_{s,n'r}(q,k)G_r^{m'}(k)\widehat{T}_{rn}^{m'm}(k,p)\,, \tag{D.11}$$

and

$$\begin{aligned}\widehat{T}_t &= \sum_r \int \frac{\mathrm{d}k}{2\pi}\,\frac{1}{2}\widehat{V}_{t,n'r}(q,k)G_r^{m'+1}(k)\widehat{T}_{rn}^{(m'+1)m}(k,p) \\ &+ \sum_r \int \frac{\mathrm{d}k}{2\pi}\,\frac{1}{2}\widehat{V}_{t,n'r}(q,k)G_r^{m'-1}(k)\widehat{T}_{rn}^{(m'-1)m}(k,p)\,.\end{aligned} \tag{D.12}$$

Using Eq. (D.8) for the poles in the Green's function yields

$$\begin{aligned}\widehat{T}_s = &\sum_{r=Propagating}\int_0^\infty \frac{\widehat{V}_{s,n'r}(q,k)\widehat{T}^{m'm}_{rn}(k,p) - \widehat{V}_{s,n'r}(q,k_r^{m'})\widehat{T}^{m'm}_{rn}(k_r^{m'},p)}{(k_r^{m'})^2-k^2}\frac{\mathrm{d}k}{2\pi}\\ &+\sum_{r=Propagating}\int_0^\infty \frac{\widehat{V}_{s,n'r}(q,-k)\widehat{T}^{m'm}_{rn}(-k,p) - \widehat{V}_{s,n'r}(q,-k_r^{m'})\widehat{T}^{m'm}_{rn}(-k_r^{m'},p)}{(k_r^{m'})^2-k^2}\frac{\mathrm{d}k}{2\pi}\\ &-\sum_{r=Propagating}\frac{i}{4|k_r^{m'}|}(\widehat{V}_{s,n'r}(q,k_r^{m'})\widehat{T}^{m'm}_{rn}(k_r^{m'},p)+\widehat{V}_{s,n'r}(q,-k_r^{m'})\widehat{T}^{m'm}_{rn}(-k_r^{m'},p))\\ &-\sum_{r=non-Propagating}\int_{-\infty}^\infty \frac{\mathrm{d}k}{2\pi}\frac{\widehat{V}_{s,n'r}(q,k)\widehat{T}^{m'm}_{rn}(k,p)}{(\kappa_r^{m'})^2+k^2}.\end{aligned} \tag{D.13}$$

Notice that we have split the sum over the subbands into two sums, one over propagating modes and another over non-propagating modes. This is done because the Green's function is not singular for the non-propagating modes. The wavevector is an imaginary number in those cases and we have emphasised this by writing $\kappa_r^{m'} = ik_r^{m'}$. The next step is to turn the integrals into sums by evaluating the integral at points k_j with corresponding weight w_j. The index j runs from 1 to N_g, where N_g is the number of points in the integration.

$$\begin{aligned}\widehat{T}_s = &\sum_{r=Propagating}\sum_{j=1}^{N_g} \frac{\widehat{V}_{s,n'r}(q,k_j)\widehat{T}^{m'm}_{rn}(k_j,p) - \widehat{V}_{s,n'r}(q,k_r^{m'})\widehat{T}^{m'm}_{rn}(k_r^{m'},p)}{(k_r^{m'})^2-k^2}\frac{\omega_j'}{2\pi}\\ &+\sum_{r=Propagating}\sum_{j=1}^{N_g} \frac{\widehat{V}_{s,n'r}(q,-k_j)\widehat{T}^{m'm}_{rn}(-k_j,p) - \widehat{V}_{s,n'r}(q,-k_r^{m'})\widehat{T}^{m'm}_{rn}(-k_r^{m'},p)}{(k_r^{m'})^2-k_j^2}\frac{\omega_j'}{2\pi}\\ &-\sum_{r=Propagating}\frac{i}{4|k_r^{m'}|}(\widehat{V}_{s,n'r}(q,k_r^{m'})\widehat{T}^{m'm}_{rn}(k_r^{m'},p)+\widehat{V}_{s,n'r}(q,-k_r^{m'})\widehat{T}^{m'm}_{rn}(-k_r^{m'},p))\\ &-\sum_{r=non-Propagating}\sum_{j=1}^{N_g}\frac{\omega_j'}{2\pi}\frac{\widehat{V}_{s,n'r}(q,k_j)\widehat{T}^{m'm}_{rn}(k_j,p)}{(\kappa_r^{m'})^2+k_j^2}\\ &-\sum_{r=non-Propagating}\sum_{j=1}^{N_g}\frac{\omega_j'}{2\pi}\frac{\widehat{V}_{s,n'r}(q,-k_j)\widehat{T}^{m'm}_{rn}(-k_j,p)}{(\kappa_r^{m'})^2+k_j^2}.\end{aligned} \tag{D.14}$$

We now make a Gauss-net for a four point Gaussian integration [27, 30],

$$q_j = \begin{cases} -k_{N_g-j+1} & j=1,\ldots,N_g\\ k_{j-N_g} & j=N_g+1,\ldots,2N_g,\end{cases} \tag{D.15}$$

and for the weights

$$\omega_j = \begin{cases} \frac{\omega'_{N_g-j+1}}{2\pi} & j=1,\ldots,N_g\\ \frac{\omega'_{j-N_g}}{2\pi} & j=N_g+1,\ldots,2N_g,\end{cases} \tag{D.16}$$

resulting in

$$\begin{aligned}\widehat{T}_s = &\sum_{r=Propagating}\sum_{j=N_g+1}^{2N_g}\omega_j\frac{\widehat{V}_{s,n'r}(q,k_j)\widehat{T}^{m'm}_{rn}(k_j,p)-\widehat{V}_{s,n'r}(q,k_r^{m'})\widehat{T}^{m'm}_{rn}(k_r^{m'},p)}{(k_r^{m'})^2-k_j^2}\\
&+\sum_{r=Propagating}\sum_{j=1}^{N_g}\omega_j\frac{\widehat{V}_{s,n'r}(q,k_j)\widehat{T}^{m'm}_{rn}(k_j,p)-\widehat{V}_{s,n'r}(q,-k_r^{m'})\widehat{T}^{m'm}_{rn}(-k_r^{m'},p)}{(k_r^{m'})^2-k_j^2}\\
&-\sum_{r=Propagating}\frac{i}{4|k_r^{m'}|}(\widehat{V}_{s,n'r}(q,k_r^{m'})\widehat{T}^{m'm}_{rn}(k_r^{m'},p)+\widehat{V}_{s,n'r}(q,-k_r^{m'})\widehat{T}^{m'm}_{rn}(-k_r^{m'},p))\\
&-\sum_{r=non-Propagating}\sum_{j=1}^{2N_g}\omega_j\frac{\widehat{V}_{s,n'r}(q,k_j)\widehat{T}^{m'm}_{rn}(k_j,p)}{(\kappa_r^{m'})^2+k_j^2}\,.\end{aligned}\tag{D.17}$$

If we now collect together terms and use that $(\kappa_r^{m'})^2+k_j^2=-((k_r^{m'})^2-k_j^2)$, we obtain

$$\begin{aligned}\widehat{T}_s = &\sum_{r=All}\sum_{j=1}^{2N_g}\omega_j\frac{\widehat{V}_{s,n'r}(q,k_j)\widehat{T}^{m'm}_{rn}(k_j,p)}{(k_r^{m'})^2-k_j^2}\\
&-\sum_{r=Propagating}\widehat{V}_{s,n'r}(q,k_r^{m'})\widehat{T}^{m'm}_{rn}(k_r^{m'},p)\frac{1}{2}\left(\sum_{j=1}^{2N_g}\omega_j\frac{1}{(k_r^{m'})^2-k_j^2}+\frac{i}{2|k_r^{m'}|}\right)\\
&-\sum_{r=Propagating}\widehat{V}_{s,n'r}(q,-k_r^{m'})\widehat{T}^{m'm}_{rn}(-k_r^{m'},p)\frac{1}{2}\left(\sum_{j=1}^{2N_g}\omega_j\frac{1}{(k_r^{m'})^2-k_j^2}+\frac{i}{2|k_r^{m'}|}\right).\end{aligned}\tag{D.18}$$

The steps for T_t are the same and give

$$\begin{aligned}\widehat{T}_t = &\sum_{r=All}\sum_{j=1}^{2N_g}\frac{\omega_j}{2}\frac{\widehat{V}_{t,n'r}(q,k_j)\widehat{T}^{(m'+1)m}_{rn}(k_j,p)}{(k_r^{m'+1})^2-k_j^2}\\
&-\sum_{r=Propagating}\widehat{V}_{t,n'r}(q,k_r^{m'+1})\widehat{T}^{(m'+1)m}_{rn}(k_r^{m'+1},p)\frac{1}{4}\left(\sum_{j=1}^{2N_g}\omega_j\frac{1}{(k_r^{m'+1})^2-k_j^2}+\frac{i}{2|k_r^{m'+1}|}\right)\\
&-\sum_{r=Propagating}\widehat{V}_{t,n'r}(q,-k_r^{m'+1})\widehat{T}^{(m'+1)m}_{rn}(-k_r^{m'+1},p)\frac{1}{4}\left(\sum_{j=1}^{2N_g}\omega_j\frac{1}{(k_r^{m'+1})^2-k_j^2}+\frac{i}{2|k_r^{m'+1}|}\right)\\
&+\sum_{r=All}\sum_{j=1}^{2N_g}\frac{\omega_j}{2}\frac{\widehat{V}_{t,n'r}(q,k_j)\widehat{T}^{(m'-1)m}_{rn}(k_j,p)}{(k_r^{m'-1})^2-k_j^2}\\
&-\sum_{r=Propagating}\widehat{V}_{t,n'r}(q,k_r^{m'-1})\widehat{T}^{(m'-1)m}_{rn}(k_r^{m'-1},p)\frac{1}{4}\left(\sum_{j=1}^{2N_g}\omega_j\frac{1}{(k_r^{m'-1})^2-k_j^2}+\frac{i}{2|k_r^{m'-1}|}\right)\\
&-\sum_{r=Propagating}\widehat{V}_{t,n'r}(q,-k_r^{m'-1})\widehat{T}^{(m'-1)m}_{rn}(-k_r^{m'-1},p)\frac{1}{4}\left(\sum_{j=1}^{2N_g}\omega_j\frac{1}{(k_r^{m'-1})^2-k_j^2}+\frac{i}{2|k_r^{m'-1}|}\right),\end{aligned}\tag{D.19}$$

the equation is in principle the same as T_s with $m\to m\pm1$. We would now like to simplify the sums by reducing the number of indexes, as this makes it easier to deal the

μ	n	k
1	1	k_1
$\vdots$	$\vdots$	$\vdots$
$2N_g$	1	k_{2N_g}
$2N_g+1$	2	k_1
$\vdots$	$\vdots$	$\vdots$
$2N_{modes}N_g$	N_{modes}	k_{2N_g}
$2N_{modes}N_g+1$	1	$-k_1^m$
$2N_{modes}N_g+2$	2	$-k_2^m$
$\vdots$	$\vdots$	$\vdots$
$2N_{modes}N_g+N_p^m$	N_p^m	$-k_{N_p^m}^m$
$2N_{modes}N_g+N_p^m+1$	1	k_1^m
$\vdots$	$\vdots$	$\vdots$
$2N_{modes}N_g+2N_p^m$	N_p^m	$k_{N_p^m}^m$

Table II: The μ mapping used in the numerical calculations.
Based on: J. H. Bardarson, Master's thesis, University of Iceland, 2004 [27].

equation numerically. In Table. II we see a mapping of the summation indexes (n, k) to a single index (μ). Writing the equations using this new index yields

$$\begin{aligned}\widehat{T}_{n'n}^{m'm}(q,p) = \widehat{V}_{s,n'n}^{m'}(q,p)\delta_{m'-m,0} + \frac{1}{2}V_{t,n'n}(q,p)(\delta_{m'-m,-1}+\delta_{m'-m,1}) \\ + \left(\sum_{\mu=1}^{2N_{modes}N_g} + \sum_{2N_{modes}N_g+2\sum N_p^{m'-1}+1}^{2N_{modes}N_g+2\sum N_p^{m'}}\right) D_\mu^{m'}\widehat{V}_{s,n'\mu}(q)T_{\mu n}^{m'm}(p) \\ + \left(\sum_{\mu=1}^{2N_{modes}N_g} + \sum_{2N_{modes}N_g+2\sum N_p^{m'}+1}^{2N_{modes}N_g+2\sum N_p^{m'+1}}\right) \frac{1}{2}D_\mu^{m'}\widehat{V}_{t,n'\mu}(q)T_{\mu n}^{(m'+1)m}(p) \\ + \left(\sum_{\mu=1}^{2N_{modes}N_g} + \sum_{2N_{modes}N_g+2\sum N_p^{m'-2}+1}^{2N_{modes}N_g+2\sum N_p^{m'-1}}\right) \frac{1}{2}D_\mu^{m'}\widehat{V}_{t,n'\mu}(q)T_{\mu n}^{(m'-1)m}(p)\,, \end{aligned} \tag{D.20}$$

where the function $D_\mu^{m'}$ has been defined in the following way

$$D_\mu^{m'} = \begin{cases} \omega_j \frac{1}{(k_r^{m'})^2-k_j^2} & \mu = 1,\ldots,2N_{modes}N_g\,, \\ & r = \text{All modes}, \\ -\frac{1}{2}\left(\sum_{j=1}^{2N_g}\left(\omega_j\frac{1}{(k_r^{m'})^2-k_j^2}\right) + \frac{i}{2|k_r^{m'}|}\right) & \mu = 2N_{modes}N_g+1,\ldots,2N_{modes}N_g+2\sum N_p^{M_{max}}\,, \\ & r = \text{Propagating modes}. \end{cases} \tag{D.21}$$

D.3 Structure of the Matrix

Equation (D.20) gives us hints of how it should be structured into a matrix for numerical calculations. If the sideband index where removed the equation would be the same as in the static case, i.e. the matrix should reduce to the static case for a static potential. This would suggest that each sideband m should give a sub-matrix containing the Gauss-net and the subband sum for that m. The coupling of the sidebands also gives another clue, as each sideband is only coupled to its adjacent bands the matrix should have a tri-diagonal form. The end result is a matrix that has a block tri-diagonal structure. An example for $M_{max} = 5$ is given in Fig. D.1. It shows how the sub-matrices are structured into the overall matrix and how the coupling between the sidebands is cut. The size of

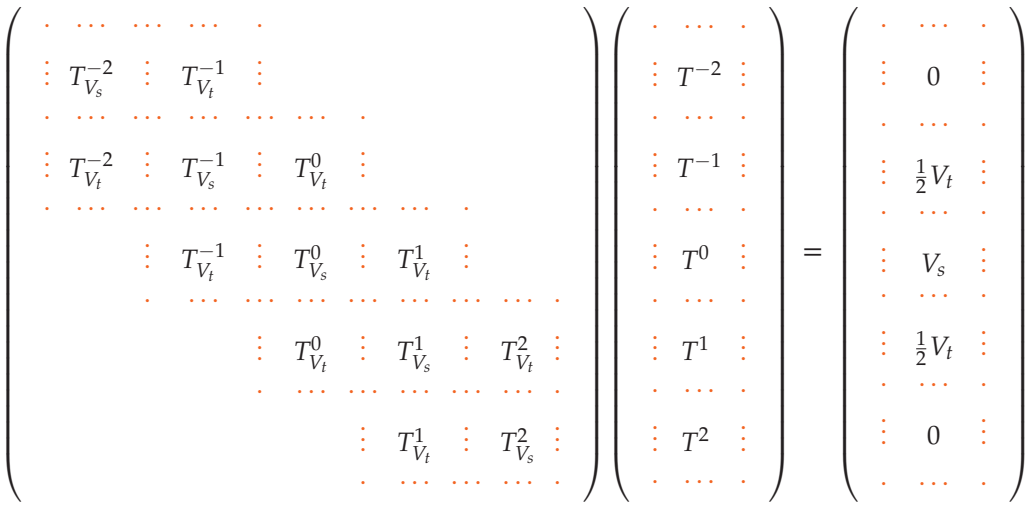

FIG. D.1: Structure of the matrix used in the numerical calculations.

a sub-matrix is $\{2N_{modes}N_g + 2N_p\} \times \{2N_{modes}N_g + 2N_p\}$, i.e. two times the Gauss-net ($2N_g$) multiplied with the number of subband in the calculations, plus two times the number propagating modes ($2N_p$). The reason why the Gauss-net and the propagating modes are multiplied with two is to also take into account negative numbers. The whole matrix has the size $\{M_{max}(2N_{modes}N_g + 2N_p)\} \times \{M_{max}(2N_{modes}N_g + 2N_p)\}$. In order to obtain a square matrix there must be an equal number of positive and negative sidebands. Therefore, M_{max} is always of the form $M_{max} = 1 + 2s$ where $s \in \mathbb{N}_0$. There is also a physical reason to have an equal number of sideband on each side. If a potential is capable of giving an electron the energy $m\hbar\omega$ it should also be capable of taking it away.

Bibliography

[1] J. H. Bardarson, I. Magnusdottir, G. Gudmundsdottir, C.-S. Tang, A. Manolescu, and V. Gudmundsson, *Coherent electronic transport in a multimode quantum channel with Gaussian-type scatterers*, Phys. Rev. B **70**, 245302 (2004). 1, 15, 18

[2] P. F. Bagwell, *Evanescent modes and scattering in quasi-one-dimensional wires*, Phys. Rev. B **41**, 10354 (1990). 1, 11

[3] V. Gudmundsson, Y.-Y. Lin, C.-S. Tang, V. Moldoveanu, J. H. Bardarson, and A. Manolescu, *Transport through a quantum ring, dot, and barrier embedded in a nanowire in a magnetic field*, Phys. Rev. B **71**, 235302 (2005). 1, 8, 40

[4] O. Valsson, C.-S. Tang, and V. Guðmundsson, *Coherent switching by detuning a side-coupled quantum-dot system*, Phys. Rev. B **78**, 165318 (2008). 1

[5] J. H. Shirley, *Solutions of the Schrödinger Equation with a Hamiltonian Periodic in Time*, Phys. Rev. **138**, B979 (2008). 2, 4, 8

[6] D. J. Thouless, *Quantization of particle transport*, Phys. Rev. B **27**, 6083 (1983). 2

[7] H. Bruus and K. Flensberg, *Many-Body Quantum Theory in Condensed Matter Physics, An Introduction* (Oxford University Press, 2004). 2

[8] S. A. Gurvitz, *Resonant scattering on impurities in the quantum Hall effect*, Phys. Rev. B **51**, 7123 (1995). 7, 45, 50

[9] D. J. Griffiths, *Introduction to Quantum Mechanics, 2nd ed.* (Pearson Prentice Hall, 2005).

[10] P. F. Bagwell and R. K. Lake, *Resonance in transmission through an oscillating barrier*, Phys. Rev. B **46**, 15329 (1992). 13, 15

[11] C. S. Chu and C. S. Tang, *Effects of a time-dependent transverse electric field on the quantum transport in narrow channels*, Solid State Communications **97**, 119 (1996).

[12] C. S. Tang and C. S. Chu, *Quantum transport in the presence of a finite-rang time-modulated potential*, Phys. Rev. B **53**, 4838 (1996). 13

[13] B. J. van Wees, H. van Houten, C. W. J. Beenakker, J. G. Williamson, L. P. Kouwenhoven, D. van der Marel, and C. T. Foxon, *Quantized Conductance of Point Contacts in a Tow-Dimensional Electron Gas*, Phys. Rev. Lett. **60**, 848 (1988). 23, 30

[14] M. Büttiker, *Quantized transmission of a saddle-point constriction*, Phys. Rev. B **41**, 7906 (1990). 23

[15] B. J. van Wees, L. P. Kouwenhoven, C. J. P. M. Harmans, J. G. Williamson, C. E. Timmering, M. E. I. Broekaart, C. T. Foxon, and J. J. Harris, *Observation of zero-dimensional states in a one-dimensional electron interferometer*, Phys. Rev. Lett. **62**, 2523 (1989). 26

[16] F. E. Camino, W. Zhou, and V. J. Goldman, *Aharonov-Bohm electron interferometer in the integer quantum Hall regime*, Phys. Rev. B **72**, 155313 (2005).

[17] S. Ihnatsenka and I. V. Zozoulenko, *Interacting electrons in the Aharonov-Bohm interferometer*, Phys. Rev. B **77**, 235304 (2008). 26

[18] V. Gudmundsson, C. Gainar, C.-S. Tang, V. Moldoveanu, and A. Manolescu, *Time-dependent transport via the generalized master equation through a finite quantum wire with an embedded subsystem*, arXiv:0903.3491v1 [cond-mat.mes-hall] (2009). 28

[19] Y. Aharonov and D. Bohm, *Significance of Electromagnetic Potentials in the Quantum Theory*, Phys. Rev. **115**, 485 (1959). 28

[20] Y. Aharonov and D. Bohm, *Further Considerations on Electromagnetic Potentials in the Quantum Theory*, Phys. Rev. **123**, 1511 (1961). 28

[21] P. H. M. van Lossdrecht, C. W. J. Beenakker, H. V. Houten, J. G. Williamson, B. J. van Wees, J. E. Mooij, C. T. Foxon, and J. J. Harris, *Aharonov-Bohm effect in a singly connected point contact*, Phys. Rev. B **38**, 10162 (1988). 30

[22] C. Cohen-Tannoudji, B. Diu, and F. Laloë, *Quantum Mechanics* (Hermann and John Wiley & Sons, 1977). 50

[23] M. R. Spiegel and J. Liu, *Mathematical Handbook of Formulas and Tables, 2d ed.* (McGraw-Hill, 1999). 50

[24] I. S. Ryzhik and I. M. Gradshteyn, *Table of Integrals, Series, and Products, 6th edition* (Academic Press, 2000). 54

[25] S. Kohler, J. Lehmann, and P. Hänggi, *Driven quantum transport on the nanoscale*, Phys. Rep. **4**06, 379 (2005). 57

[26] D. L. Lukes, *Differential Equations: Classical to Controlled* (Academic Press, INC., 1982). 57

[27] J. H. Bardarson, Master's thesis, University of Iceland, 2004. 61, 63, 65

[28] A. L. Fetter and J. D. Walecka, *Quantum Theory of Many-Particle Systems* (Dover Publications, INC., 1971). 61

[29] G. B. Arfken and H. J. Weber, *Mathematical Methods for Physicists* (Elsevier Academic Press, 2005). 61

[30] M. Abramowitz and I. A. Stegun, *Handbook of Mathematical Functions: with Formulas, Graphs, and Mathematical Tables* (Dover Publications, 1965). 63

[31] B. Bradie, *A Friendly Introduction to Numerical Analysis* (Pearson Education, Inc., 2006).